Reconstruction of thiospinel to active sites and spin channels for water oxidation

Tianze Wu, Yuanmiao Sun, Xiao Ren, Jiarui Wang, Jiajia Song, Yangdan Pan, Yongbiao Mu, Jianshuo Zhang, Qiuzhen Cheng, Guoyu Xian, Shibo Xi, Chengmin Shen, Hong-Jun Gao, Adrian C. Fisher, Matthew P. Sherburne, Yonghua Du, Günther G. Schere, Joel W. Ager, Jose Gracia, Haitao Yang, Lin Zeng, Zhichuan J. Xu**

Dr T. Wu, Dr Y. Sun, Dr. X. Ren, J. Wang, Dr J. Song, Prof Z. J. Xu
School of Materials Science and Engineering, Nanyang Technological University, 50 Nanyang Avenue, 639798, Singapore
E-mail: xuzc@ntu.edu.sg
Y. Pan, Y. Mu, J. Zhang, Prof L. Zeng
Department of Mechanical and Energy Engineering, Southern University of Science and Technology, Shenzhen, Guangdong, 518055, China
E-mail: zengl3@sustech.edu.cn
Q. Cheng, G. Xian, C. Shen, Prof H. Yang, H. J. Gao
Beijing National Laboratory for Condensed Matter Physics and Institute of Physics, Chinese Academy of Science, Beijing 100190, China
Dr S. Xi
Institute of Sustainability for Chemicals, Energy and Environment, A*STAR, 1 Pesek Road, 627833, Singapore
Prof A. C. Fisher
Department of Chemical Engineering, University of Cambridge, Cambridge CB2 3RA, UK
Prof A. C. Fisher
The Cambridge Centre for Advanced Research and Education in Singapore, 1 CREATE Way, 138602, Singapore
M. P. Sherburne, Prof J. W. Ager
Department of Materials Science and Engineering, University of California at Berkeley, Berkeley, California 94720, USA;
M. P. Sherburne, Prof J. W. Ager
Berkeley Educational Alliance for Research in Singapore Ltd., 1 CREATE Way, Singapore 138602, Singapore
Dr Y. Du

National Synchrotron Light Source II, Brookhaven National Laboratory, Upton, NY 11973, United States
G. G. Scherer
Talackerstr. 9 B, 5607 Hägglingen, Switzerland
Dr J. Gracia
MagnetoCat SL, General Polavieja 9 3I, 03012 Alicante, Spain

Keywords: pre-catalyst, spin channel, electrochemical reconstruction, thiospinel sulfide, oxygen evolution reaction, membrane electrode assembly

Water electrolysis is a promising technique for carbon neutral hydrogen production. A great challenge remains at developing robust and low-cost anode catalysts, where the slow reaction kinetics of water oxidation limits the overall electrolysis efficiency. Many pre-catalysts have been found to undergo surface reconstruction to give high intrinsic activity in oxygen evolution reaction (OER). The reconstructed oxyhydroxides on the surface are active species and most of them outperform directly synthesized oxyhydroxides. The reason for the high intrinsic activity remains to be explored. Here, we report a study to showcase the unique reconstruction behaviors of a pre-catalyst, thiospinel $CoFe_2S_4$, and its reconstruction chemistry for a high OER activity. The reconstruction of $CoFe_2S_4$ gives a mixture with both Fe-S component and active oxyhydroxide ($Co(Fe)O_xH_y$) because Co is more inclined to reconstruct as oxyhydroxide, while the Fe is more stable in Fe-S component in a major form of Fe_3S_4. The interface spin channel is demonstrated in the reconstructed $CoFe_2S_4$, and it optimizes the energetics of OER steps on $Co(Fe)O_xH_y$ species as well as facilitates the spin-sensitive electron transfer to reduce the kinetic barrier of O-O coupling for ground-state O_2 turnover. The advantage of using this pre-catalyst is also demonstrated in a membrane electrode assembly (MEA) electrolyzer. This work introduces the feasibility of engineering the reconstruction chemistry of the pre-catalyst for high performance and durable MEA electrolyzers.

1. Introduction

Reducing carbon emissions toward a carbon-free society is an essential goal for human beings. Hydrogen has been long promised as an alternative to fossil fuels. To realize a hydrogen energy infrastructure, the technologies for sustainable hydrogen production, such as water electrolysis using sustainable energy resources, are highly desired. One of the challenges for the implementation of water electrolyzers is the development of robust and low-cost catalysts for oxygen evolution reaction (OER), where the major energy loss in water electrolysis is given.[1] To overcome this challenge, the oxides consisting of first-row transition metals have been extensively studied in recent years and the design principles for achieving better OER efficiency have been discovered.[2] One important progress is about the active site recognition for those most efficient oxide catalysts. Some of them were found to undergo reconstruction to form active oxyhydroxides for catalyzing the OER.[3] For example, the high activity arises from di-μ-oxo bridged Co-Co sites in Co-based oxyhydroxides, where the deprotonation process leads to the generation of the active oxygen ligand.[4] Therefore, to take the advantage of the reconstruction, more effort has now been made to explore reconstructable pre-catalysts and study their performance.[5] However, one critical question has not been addressed, i.e. why a pre-catalyst is needed, instead of using the oxyhydroxide directly as the catalyst, which has been found the active phase during OER.[6] In fact, the OER activity was found different between the reconstructed oxyhydroxides and those directly-prepared oxyhydroxides.[7] And the difference was found as well among the reconstructed oxyhydroxides by different pre-catalysts.[3b, 8] The origin of such difference has not been given attention due to the lack of detailed information on the chemistry of the reconstructed catalysts as well as the reconstruction behaviors under the OER condition.

Here, we reveal the reconstruction chemistry of a thiospinel pre-catalyst ($CoFe_2S_4$) and its magnetic property after the reconstruction. The reconstruction not only results in the formation of the OER active component oxyhydroxide ($Co(Fe)O_xH_y$), but also Fe-S component (Fe_3S_4). The intrinsic activity of derived $Co(Fe)O_xH_y$ in the reconstructed phase is found higher than directly prepared one by one order of magnitude. We have investigated the difference in the ability of $CoFe_2S_4$ and $CoFe_2O_4$ towards reconstruction. The (M-S) bonding states are revealed closer to the lower-Hubbard band (LHB) in energy level than (M-O) bonding states. The electrons can be more easily removed from (M-S) bonding states than from (M-O) bonding states to result in anionic redox, which induces more structural flexibility in sulfides for reconstruction. In $CoFe_2S_4$, (Co-S) bonding states show a much higher energy level than (Fe-

S) bonding states, which leads to different reconstruction behaviours of Co and Fe species. In reconstructed $CoFe_2S_4$, Co is found in oxyhydroxide phase $Co(Fe)O_xH_y$, while Fe is more stable in Fe-S components in the forms of greigite Fe_3S_4. It is consistent with the fact that $Ksp(Fe_3S_4)$ is lower than $Ksp(Fe(OH)_3)$ in alkaline.

The reconstruction creates abundant $Fe_3S_4/Co(Fe)O_xH_y$ interfaces, where a remarkable exchange bias can be found. It indicates the existence of a spin-polarized interface that serves as the spin channel. Such interface spin channel is further demonstrated by DFT study using a $Co_{0.8}Fe_{0.2}OOH@Fe_3S_4$ interfacial model, in which more net spins and higher magnetizations of atoms are found for $Co_{0.8}Fe_{0.2}OOH$ paired with Fe_3S_4. The modified magnetic structure of $Co_{0.8}Fe_{0.2}OOH$ gives optimized energetics of OER steps. Moreover, the polarized spins in spin channels can facilitate the spin polarization process in OER which was believed critical for fast kinetics toward O_2 turnover in its ground state.[9] In OER steps, O-O coupling with a high kinetic (or energetic) barrier can be a rate-determining step.[10] Under three well-established OER mechanisms, the spins in OER intermediates and the spin transfer along with OER coordinates are discussed to explain the role of the spin channel in O-O coupling. Through an analysis of the effect of the spin channel on both the energetic and kinetic barriers in all possible OER pathways, it is believed that the spin channel at $Fe_3S_4/Co(Fe)O_xH_y$ interface is responsible for the higher intrinsic activity of the reconstructed $CoFe_2S_4$ than directly prepared Co(Fe) oxyhydroxides. Moreover, the half-metal property of greigite Fe_3S_4 brings high electric conductivity to reconstructed $CoFe_2S_4$. The high intrinsic activity of reconstructed $CoFe_2S_4$ can be maintained without using conductive carbon. This advantage benefits the application in a MEA electrolyzer because the carbon support is not stable under the tough working condition of the anode. It may address a common conductivity issue that limits many directly prepared oxyhydroxide such as $NiFeO_xH_y$ for MEA electrolyzers.

2. Result and discussion

2.1. The Pre-catalyst design: thiospinel vs. spinel oxides

The pre-catalyst design is started with a Co-based oxide $CoFe_2O_4$. To promote the reconstruction of $CoFe_2O_4$ is not easy because $CoFe_2O_4$ is relatively stable under alkaline OER conditions.[11] By DFT calculations (Figure 1a), we first examined the electronic structure of $CoFe_2O_4$. Its projected density of state (pDOS) is shown in Figure 1b. The physical origin of

the limited reconstruction of $CoFe_2O_4$ is from a low O 2p level relative to Fermi level, which limits the structural flexibility of oxides.[12] For promoting the reconstruction of oxides, it has been proposed previously to uplift the O 2p level by the cation substitution.[13] Thus, the lattice oxygens can be involved in OER to induce certain structural flexibility for reconstruction.[11] Here, as compared to $CoFe_2O_4$, $CoFe_2S_4$ is easier to enable the reconstruction. The DFT study shows a notable advantage of Co-S hybridization over Co-O hybridization toward realizing reconstruction. The pDOS of $CoFe_2S_4$ is shown in Figure 1b (the details are summarized in Table S1). The S 3p band of $CoFe_2S_4$ exhibits a notable higher energy level and its center is closer to the Fermi level than the O 2p in $CoFe_2O_4$. Moreover, for later transition metal oxides/sulfides, (M-O)*/(M-S)* orbitals tend to be split by strong d-d orbital interactions, resulting in one empty upper-Hubbard band (UHB) and one filled lower-Hubbard band (LHB)[7a, 14]. In an anodic sweep, the electrons will be removed from the LHB firstly, resulting in an increasing oxidation state of metal cations. In many stable oxides (under the alkaline OER condition), like $CoFe_2O_4$, the (M-O) orbital is low in energy.[15] Thus, the oxidation of OH^- would follow the oxidation of metal cations without compromising the stability of M-O bonds in these oxides. As a result, we can see a stable redox of Co^{2+}/Co^{3+} at potential of ~1.1 V in the cyclic voltammetry (CV) of $CoFe_2O_4$ (Figure S1a), which indicates the electron could be only removed from LHB below E_F. As the O 2p is low in energy relative to Fermi level in $CoFe_2O_4$, the (Co-O)* exhibits less oxygen character which implies the difficulty in lattice oxygen oxidation along with the removal of the electron from LHB. Without lattice oxygen oxidation in OER, there is limited structural flexibility in $CoFe_2O_4$ to undergo reconstruction under alkaline OER. However, as S 3p state in the sulfide is at a higher energy level than O 2p state in oxides, the (M-S) orbitals are closer to LHB than (M-O) orbitals (Figure 1c). Thus, following the oxidation of metal cations, the electrons could be removed from (M-S) bonding orbitals along the anodic sweep before the oxidation of OH^-, which results in the breaking of M-S bonds and facilitates the formation of oxyhydroxides before the OER.[16]

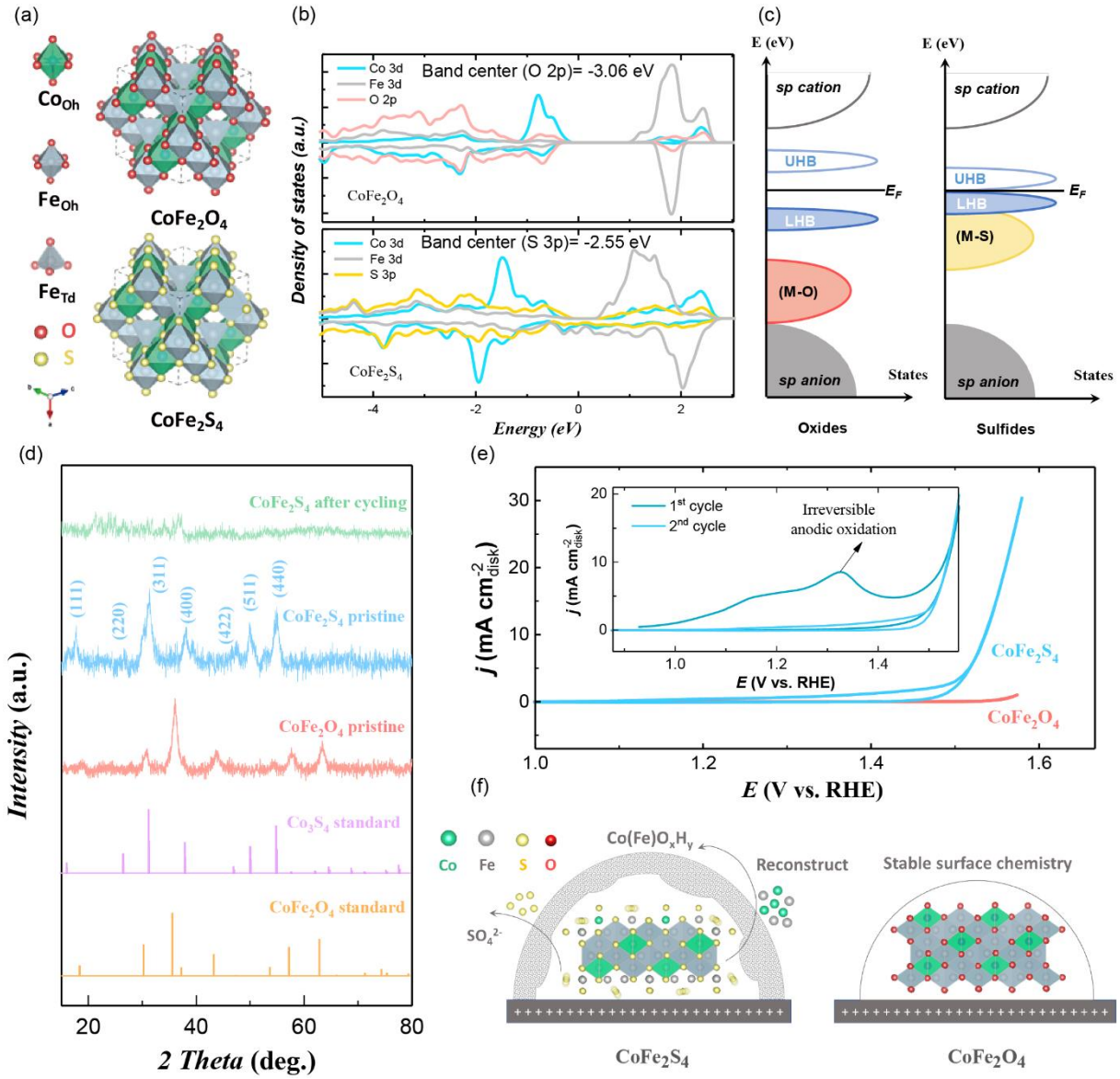

Figure 1. A theoretical reconnaissance for pre-catalyst design and experimental demonstration. a) The computational models of $CoFe_2O_4$ and $CoFe_2S_4$. b) The computed projected density of state (pDOS) of $CoFe_2O_4$ and $CoFe_2S_4$. The calculated energy is referenced to the Fermi level. c) Schematic energy bands of $CoFe_2O_4$ and $CoFe_2S_4$ relative to the Fermi level in consideration of Mott–Hubbard splitting. d) The powder X-ray diffraction (XRD) patterns of as-prepared $CoFe_2O_4$, $CoFe_2S_4$, and $CoFe_2S_4$ after cycling. e) The cyclic voltammetry (CV) curves of $CoFe_2S_4$ and $CoFe_2O_4$ in O_2-saturated 1 M KOH with a scan rate of 10 mV s^{-1}. The inset panel shows the 1st and 2nd cycles of $CoFe_2S_4$. f) The schematic illustration of the reconstruction of $CoFe_2S_4$ to generate active oxyhydroxides on the surface.

The $CoFe_2S_4$ was synthesized via a hydrothermal method and the $CoFe_2O_4$ was prepared by a sol-gel method. The spinel structure of as-synthesized $CoFe_2S_4$ and $CoFe_2O_4$ has been confirmed by powder X-ray diffraction (XRD) (Figure 1d), where the diffraction peaks match the standard patterns. Figure 1e shows the OER CVs of $CoFe_2S_4$ and $CoFe_2O_4$ in O_2-saturated 1.0 M KOH. The inset presents the 1st and 2nd CV cycles of $CoFe_2S_4$. The reconstruction behaviour of $CoFe_2S_4$ in 1st cycle is notable, where the irreversible anodic oxidation in 1st cycle is attributed to the oxidation of (M-S) and indicates the reconstruction. However, for $CoFe_2O_4$, negligible difference could be found between the 1st and the 2nd CV cycle (Figure S1a). Its surface chemistry remains stable under alkaline OER as indicated by the stable profiles of CV in subsequent 500 cycles (Figure S1b) and the HRTEM images before and after cycling (Figure S1c and 1d). The reconstruction of $CoFe_2S_4$ greatly benefits the OER activity. As seen in the OER CVs in Figure 1e, the OER activity of reconstructed $CoFe_2S_4$ is much higher than that of $CoFe_2O_4$. Tafel plots of $CoFe_2S_4$ and $CoFe_2O_4$ show that the reconstructed $CoFe_2S_4$ can deliver an activity ~two orders of magnitude higher than $CoFe_2O_4$ (Figure S2). In the reconstruction of $CoFe_2S_4$, the Co and Fe cations can reconstruct on the surface to form $Co(Fe)O_xH_y$ species which provides active sites toward OER (Figure 1f). Further, both CV cycling and chronoamperometry can lead to the reconstruction of $CoFe_2S_4$, which results in similar OER performance after complete reconstruction (Figure S3).

Figure 2a shows the TOF values of the reconstructed $Co(Fe)O_xH_y$ from $CoFe_2S_4$, the benchmark Co(Fe)OOH, and other state-of-art catalysts. The bottom symbol refers to the TOF by assuming all metal atoms in the catalyst are effective (denoted as “bulk”) and the upper one refers to the TOF by calculating only the active metal atoms on the surface (denoted as “surface”). The reconstruction of pre-catalysts will increase the surface area of catalysts by generating nano-sized structures. Thus, it is necessary to give a comparison of TOF on a per-surface-site basis which presents the intrinsic activity of reconstructed oxyhydroxide independent to the surface

area of catalysts. It is notable that the reconstructed $Co(Fe)O_xH_y$ from $CoFe_2S_4$ shows an outstanding $TOF_{surface}$ of ~ 1 order of magnitude higher than directly-prepared $Co_{0.8}Fe_{0.2}(OOH)$ in literature,[17] which demonstrates higher intrinsic activity of the reconstructed $Co(Fe)O_xH_y$ toward OER. Other reported pre-catalysts in Co(Fe) sulfides (e.g. Co_3S_4 and Fe_2CoS_y)[18] much underperform the reconstructed $CoFe_2S_4$ in TOF_{bulk}. The reconstructed $Co(Fe)O_xH_y$ can deliver much higher intrinsic activity than $Ba_{0.5}Sr_{0.5}Co_{0.8}Fe_{0.2}O_{3-\delta}$ (BSCF), which was found to undergo surface reconstruction in alkaline OER as well.[3b, 19] The intrinsic activity is also higher than "Co-Pi" (*in-situ* evolved active Co oxo species).[20] Its intrinsic activity is comparable to $NiFeO_xH_y$/ Au (among the highest reported to date)[21]. From the above activity comparison, the superior activity of the reconstructed $CoFe_2S_4$ is believed to rely on a unique reconstruction behavior which could be different from other referenced Co(Fe) sulfide pre-catalysts. This also implies that the advantage of pre-catalysts over directly-prepared oxyhydroxide is not restricted to the nano-structuration during reconstruction but should involve specific chemistry closely associated with the high intrinsic activity of reconstructed oxyhydroxides. We also examined if the adsorbed SO_4^{2-} on the surface of catalyst greatly affects the OER activity, which was previously demonstrated for Ni oxyhydroxide.[22] The $CoFe_2S_4$ electrode after reconstruction was rinsed with fresh electrolyte and then tested in the fresh electrolyte, which aims to clean the soluble SO_4^{2-} adsorbed on the surface. The OER CVs before and after such operations are shown in Figure S4. Very limited activity difference is found by reducing the amount of adsorbed SO_4^{2-}, which indicates that the decoration of SO_4^{2-} may not greatly affect the rate-determining step in this case. But further attention should still be paid on the possible effect from SO_4^{2-} decoration for other thiospinel pre-catalysts because it may serve as a proton adaptor to affect the deprotonation process on the oxyhydroxide.

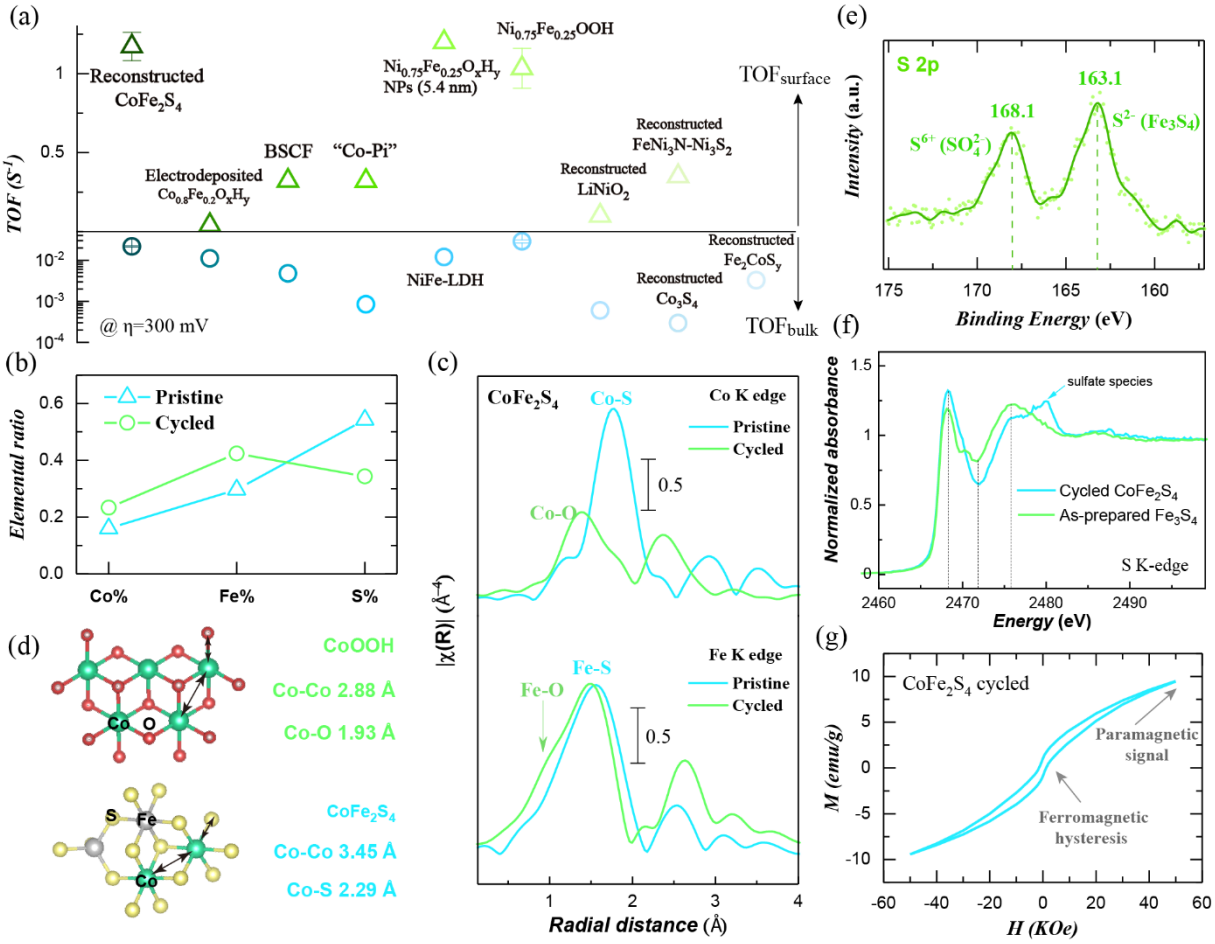

Figure 2. Critical chemistry in reconstructed $CoFe_2S_4$ associated with high intrinsic activity. a) The turnover frequency (TOF) of the reconstructed $CoFe_2S_4$, reconstructed Co_3S_4,[18a] electrodeposited $Co_{0.8}Fe_{0.2}O_xH_y$,[17] $Ba_{0.5}Sr_{0.5}Co_{0.8}Fe_{0.2}O_{3-\delta}$ film,[19] electrodeposited cobalt hydroxide ("Co-Pi"),[20] $Ni_{0.75}Fe_{0.25}O_xH_y$ NPs on Au electrode,[21] NiFe LDH[23], as-synthesized $Ni_{0.75}Fe_{0.25}OOH$ on Au electrode, reconstructed $LiNiO_2$,[24] reconstructed $FeNi_3N$-Ni_3S_2,[25] reconstructed Fe_2CoS_y[18b] . The TOF is evaluated as described in Method in details. The bottom bound refers to the TOF by assuming all metal atoms in the catalyst are effective (denoted as "bulk") and the upper one refers to the TOF by calculating only the active metal atoms on the surface (denoted as "surface"). The error bars represent the standard deviation from three independent measurements. b) The elemental ratio of Co, Fe, and S in pristine and cycled $CoFe_2S_4$, which is determined by ICP-OES measurement. c) The Fourier transform (FT) k3χ(R) Fe K-edge and Co K-edge EXAFS of $CoFe_2S_4$ before and after cycling. d) The different local atomic structures of Co in CoOOH and $CoFe_2S_4$. e) The X-ray photoelectron spectroscopy (XPS) results of S 2p of reconstructed $CoFe_2S_4$. f) The S K-edge XANES of reconstructed $CoFe_2S_4$ and Fe_3S_4. Minor sulfate species in reconstructed $CoFe_2S_4$ were generated under

electrochemical oxidation. g) The magnetic property of the $CoFe_2S_4$ after cycling (reconstruction) under 300 K.

2.2. Distinguished reconstruction behaviours in $CoFe_2S_4$

To better understand the reconstruction of $CoFe_2S_4$, the chemistry of reconstructed $CoFe_2S_4$ was then investigated. The $CoFe_2S_4$ was cycled for 50 cycles until there is no further irreversible oxidation to ensure a complete reconstruction (Figure S5). In CVs, it is noticed that the pseudocapacitive charge attributed to the irreversible oxidation has been negligible since the 5th cycle. The XRD (Figure 1d) and TEM (Figure S6a and 6b) results of $CoFe_2S_4$ before and after cycling confirm that the crystalline $CoFe_2S_4$ has collapsed and reconstructed. The reconstruction is enabled by the electrochemical anodic oxidation, while the sample immersed in O_2-saturated 1.0 M KOH for 1 hour without an applied anodic potential was found with much limited reconstruction on the surface (Figure S6c). The OER activity is almost unchanged by the pre-immersion of $CoFe_2S_4$ electrode for 1 hour (Figure S7). We also examined the elemental ratio of Co, Fe, and S in $CoFe_2S_4$ before and after reconstruction by ICP-OES (Figure 2b). The elemental ratio of S (S%) in pristine $CoFe_2S_4$ is at ~ 57%, which is consistent with the nominal elemental ratio of S in $CoFe_2S_4$. After the reconstruction, the sample was washed by Di-water and collected by centrifugation. It was still found that the S% remains at ~35%, which means around 60% lattice sulfur cannot be oxidized during the reconstruction. Hence, it is highly possible that there was another S-containing component generated after the reconstruction and was stable during OER cycles.

The local atomic structures of $CoFe_2S_4$ before and after cycling were investigated by X-ray absorption fine structure (XAFS). In Co K-edge X-ray adsorption near-edge spectra (XANES) (Figure S8), pristine $CoFe_2S_4$ exhibits a shoulder at about 7720 eV due to the existence of substantial unoccupied S p orbitals in Co circumstance.[26] This shoulder diminishes after $CoFe_2S_4$ is cycled, which implies the reconstruction of Co-S bonds. The Co k-edge extended X-ray absorption fine structure (EXAFS) (Figure 2c, top panel) further supports that Co-S bonds have nearly disappeared. Before cycling, the first-shell peak is observed at a radial distance of ~1.9 Å, while after cycling, this peak appears at a radial distance of ~1.5 Å with reduced intensity. Given that the theoretical difference of bond distance between Co-S and Co-O in spinel is ~0.36 Å (Figure 2d), the shift of the first shell peak to lower radial distance could be attributed to a nearly complete reconstruction from Co-S bonds to Co-O bonds. The intensity of the first-shell peak is reduced because the reconstructed Co-based species become more

amorphous. However, such a shift of the first-shell peak was not observed in Fe k-edge EXAFS of $CoFe_2S_4$ before and after cycling (Figure 2c, bottom panel). It was only observed an additional feature at ~1 Å that could be attributed to Fe-O bonds. Whereas, the Fe-S feature at ~1.6 Å stayed nearly unchanged after reconstruction. Thus, it is believed that the S-containing component would be Fe-S compound. The Co-S and Fe-S bonds behave differently during the reconstruction of $CoFe_2S_4$. That may originate from the nature of Co-S and Fe-S bonds in $CoFe_2S_4$. Co 3d states is at higher energy level than Fe 3d states in $CoFe_2S_4$, so that (Co-S) bonding state is closer to the LHB than (Fe-S) bonding state (Table. S1). During the anodic sweep, the electron will be easier removed from (Co-S) bonding state than from (Fe-S) bonding state (Figure S9), which results in the dominant presence of Co in the reconstructed oxyhydroxides

To identify the Fe-S component in the reconstructed $CoFe_2S_4$, the $CoFe_2S_4$ samples were firstly examined by X-ray photoelectron spectroscopy (XPS) after cycling in 1 M KOH. The XPS spectrum for S 2p is shown in Figure 2e and two states of S were detected. The sulfate signal at 168.1 eV can be ascribed to the oxidized S during the reconstruction, while the other at 163.1 eV indicates a valence state of -2 in Fe-S based sulfide. Sulfur K-edge XANES was also carried out on the reconstructed $CoFe_2S_4$ and on a synthesized Fe_3S_4 as standard (see Supplementary Note 2 for synthesis details). In Figure 2f, a major adsorption edge of reconstructed $CoFe_2S_4$ is found at energy of ~ 2468 eV, which indicates a S(-2) specie.[27] The adsorption features of the reconstructed $CoFe_2S_4$ and Fe_3S_4 are consistent as denoted in Figure 2f, except for a notable signal at ~ 2481 eV ascribed to generated sulfate species on reconstructed $CoFe_2S_4$ by electrochemical oxidation. Further, a measurement of magnetic property under 300 K was conducted. As shown in the loop in Figure 2g, clear magnetic hysteresis can be found, and the magnetization cannot reach saturated even under a high magnetic field (~60000 Oe). The generated Co-Fe (oxy)hydroxides are paramagnetic, which would be responsible for the observed unsaturated magnetization. The Fe-S component is with ferromagnetic or ferrimagnetic property. As reported, among stable sulfide compounds with S^{2-}, pyrrhotite Fe_7S_8, smythite Fe_9S_{11}, and greigite Fe_3S_4 in spinel structure with ferromagnetic or ferrimagnetic property,[28] while the mackinawite (FeS) is antiferromagnetic.[29] The spinel structure of Fe-S component is further validated by the HRTEM investigation. Moreover, the Ksp of Fe_3S_4 in alkaline is 1×10^{-101}, which is much lower than the Ksp($Fe(OH)_3$) at 1×10^{-38}. That justifies the generation of Fe_3S_4 components even in strong alkaline media. Thus, the reconstructed $CoFe_2S_4$ contains Fe-S component in a major form of greigite Fe_3S_4.

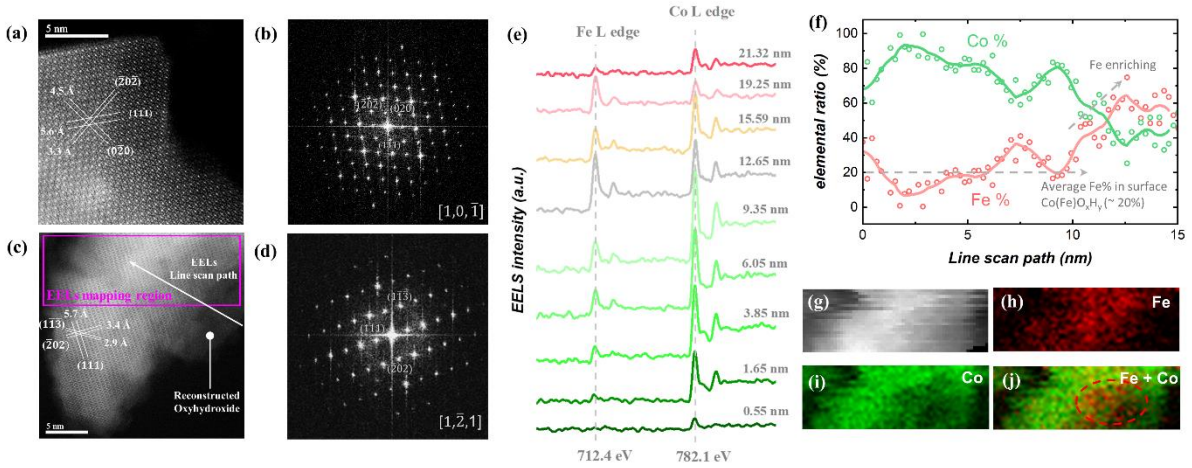

Figure 3. The HRTEM observation on the chemistry of $CoFe_2S_4$ before and after reconstruction. a-d) The HRTEM and the fast Fourier transformed (FFT) images of $CoFe_2S_4$ before (a, b) and after (c, d) cycling. The EELS line scan pathway and the EELs mapping survey region for cycled $CoFe_2S_4$ are given in Figure 3c. e) The Fe and Co L-edge EELS spectra along the line scan pathway from surface to bulk. f) The quantified elemental ratio of Co and Fe along EELS line scan pathway. g-j) The EELS mapping of selected area (purple rectangle in Figure 3c) with the survey elements of Co and Fe. The region denoted by the red circle is the Fe-rich region.

Considering the different behaviors of Co and Fe during reconstruction, the chemistry and microscopic configuration of reconstructed $CoFe_2S_4$ were further studied by HRTEM and STEM-EELS. The HRTEM images of $CoFe_2S_4$ before and after cycling are shown in Figure 3a and 3c. Their FFT patterns are shown in Figure 3b and 3d. Before the $CoFe_2S_4$ was cycled, it exhibited sheet-like morphology (Figure S6a) and was well-crystalline in spinel structure, which is consistent with the above XRD result. After the $CoFe_2S_4$ was cycled, the sheet-like morphology of $CoFe_2S_4$ collapsed (Figure S6b). The amorphous oxyhydroxide layer can be found on the surface. Most region under the surface remains the spinel structure after reconstruction as indicated in Figure 3d. To examine the local chemistry, electron energy loss spectroscopy (EELS) was carried out to probe the elemental ratio of Co and Fe in the surface and bulk regions in reconstructed products. EELS line scan was performed along a pathway from the surface to the bulk region (noted in Figure 3c). The EELS signal of Co and Fe L-edge can be identified in Figure 3e, and Figure 3f shows the quantified result of the elemental ratio of Co and Fe according to the EELS spectra. Clearly, along the scanning pathway, the Co is dominant in the surface region, while Fe is rich in the bulk region. The average elemental ratio

of Co and Fe in surface $Co(Fe)O_xH_y$ is estimated at ~ 4:1 according to EELS line scan in the oxyhydroxide surface. The EELS mapping results are shown in Figure 3g-3j. It is notable that a Fe-rich bulk is topped by a Co-rich surface. The distribution of Co and Fe elements was also checked by the EDX mapping (Figure S10) in $CoFe_2S_4$ before and after cycling. In the pristine $CoFe_2S_4$, it is confirmed that the Co and Fe are distributed evenly. After cycling, Co became enriched on the surface, leaving the bulk region rich with Fe. HRTEM and STEM-EELS results provided a picture of the reconstruction process: Co cation is inclined to leach along with anionic redox and then redeposited on the surface as oxyhydroxide species during electrochemical cycling, while Fe cations are more stable in Fe_3S_4 component remained in the bulk region.

2.3. Spin channels in the reconstructed $CoFe_2S_4$

According to the above characterizations of the reconstructed products, the reconstruction behaviour of $CoFe_2S_4$ is illustrated in Figure 4a. The Co cations are involved in a complete reconstruction into Co-Fe oxyhydroxides, accompanied by the oxidation of a part of lattice sulfur. Fe will undergo two pathways during reconstruction, where a part of Fe will reconstruct into oxyhydroxides, while the remaining Fe will reconstruct with S^{2-} to form Fe_3S_4 component. The different reconstruction behaviours of Co and Fe also lead to phase separation of the generated $Co(Fe)O_xH_y$ and Fe_3S_4 components. The $Co(Fe)O_xH_y$ is primarily in the surface region while the Fe_3S_4 is in the bulk region.

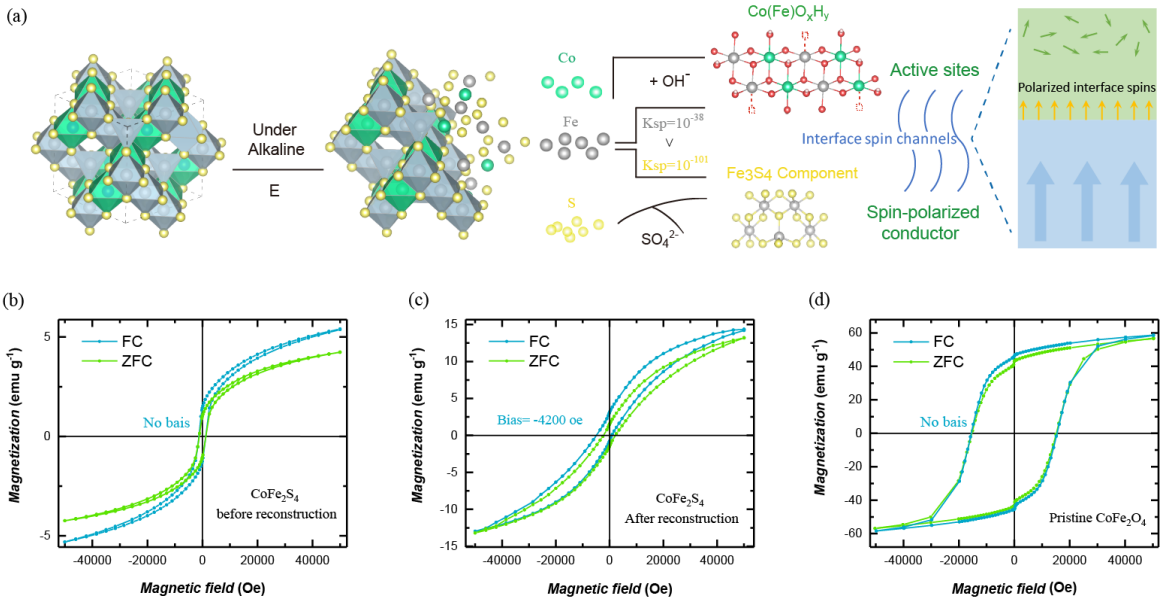

Figure 4. Spin-polarized interface in reconstructed $CoFe_2S_4$. a) The schematics of reconstruction behaviors of Co, Fe, and S elements in $CoFe_2S_4$ under alkaline OER. The K_{sp}

($Fe(OH)_3$) $\approx 10^{-38}$,[30] while the K_{sp} (Fe_3S_4) $\approx 10^{-101}$.[31] b-d) The magnetic hysteresis loop under FC and ZFC mode of (b) pristine $CoFe_2S_4$, (c) reconstructed $CoFe_2S_4$ and (d) pristine $CoFe_2O_4$. The exchange bias denotes the shift of the loop under FC mode along the x-axis. FC and ZFC denotes the cooling down process in exchange bias measurements that is with or without a magnetic field imposed. Please see details in the Method.

The reconstruction of $CoFe_2S_4$ created abundant interfaces between $Co(Fe)O_xH_y$ and Fe_3S_4 components, where a notable exchange bias effect has been detected. A standard measurement of exchange bias for $CoFe_2S_4$ before and after reconstruction was carried out, and the hysteresis loops recorded after the field-cooled (FC) or zero-field-cooled (ZFC) process are shown in Figure 4b and 4c. The loop of reconstructed $CoFe_2S_4$ with FC exhibits a negative bias of ~ -4200 Oe compared to that with ZFC process, while nearly no bias is observed in the hysteresis loop of pristine $CoFe_2S_4$. There is no bias found as well for the hysteresis loops of pristine $CoFe_2O_4$ with FC and ZFC processes (Figure 4d). It is clear that the notable exchange bias was only detected for reconstructed $CoFe_2S_4$ with abundant interfaces. The exchange bias originates from the uncompensated spins in the materials that cannot completely follow the external magnetic field, and these spins are intrinsically pinned at the interface.[32] Such interface spin pinning usually exists between two compositions in which one with ferromagnetic spins is covered by another with disordered spins, which is resulted by strong magnetic anisotropy at the interface.[33] In the reconstructed $CoFe_2S_4$, the Fe_3S_4 is neighbored by paramagnetic $Co(Fe)O_xH_y$. The spins in paramagnetic $Co(Fe)O_xH_y$ should be originally disordered but at the Fe_3S_4/$Co(Fe)O_xH_y$ interface region, the spins of $Co(Fe)O_xH_y$ can be pinned and follow the polarized spin ordering in Fe_3S_4 component, which creates interface spin channels in reconstructed $CoFe_2S_4$ (Figure 4a).

The $Co(Fe)O_xH_y$ is one of the widely reported active species for OER. With the spin pinning effect, the magnetic structure of $Co(Fe)O_xH_y$ at the interface region is modified accordingly. DFT studies were carried out to demonstrate the interfacial spin channel in $Co(Fe)O_xH_y$@Fe_3S_4 interfacial configuration. According to the elemental ratio in EELs characterization, $Co_{0.8}Fe_{0.2}OOH$ slab and $Co_{0.8}Fe_{0.2}OOH$@Fe_3S_4 interfacial models were built up as shown in Figure 5a and 5b, respectively. The projected density of states (pDOS) of $Co_{0.8}Fe_{0.2}OOH$ with and without Fe_3S_4, are shown in Figure 5c and 5d. For a fair comparison, the pDOS in Figure 5d only contains the states from $Co_{0.8}Fe_{0.2}OOH$ and all states belonging to Fe_3S_4 are excluded. With Fe_3S_4, the symmetry of electronic states in spin-up or spin-down of $Co_{0.8}Fe_{0.2}OOH$ is

greatly altered, which indicates a significant influence on the spin structure of the $Co_{0.8}Fe_{0.2}OOH$ paired with Fe_3S_4. The differences of states in spin-up and spin-down have been calculated and shown in the DOS for the two models. Paired with Fe_3S_4, more unbalanced states can be found on Co (~0.59 e^- more) atoms and on Fe (0.37e^- more) atoms in $Co_{0.8}Fe_{0.2}OOH$ layer, which increases the net spins at interface. Besides, the magnetizations of Co and Fe atoms in $Co_{0.8}Fe_{0.2}OOH$ are greatly increased by the Fe_3S_4. The magnetizations of all atoms in $Co_{0.8}Fe_{0.2}OOH$ with and without Fe_3S_4 are summarized in Table S3 and Table S4. Paired with Fe_3S_4, significant magnetization increments are found on Co and Fe atoms in $Co_{0.8}Fe_{0.2}OOH$ slab, which lifts the total magnetizations from 22.088 to 34.041. The magnetization increment indicates enhanced ferromagnetic properties of $Co_{0.8}Fe_{0.2}OOH$ at the interface region. Overall, the interface with Fe_3S_4 increases the polarization of metal atoms and provides additional net spins in $Co_{0.8}Fe_{0.2}OOH$, which is able to facilitate the spin-selective electron transfer and serves as the spin channels in OER.

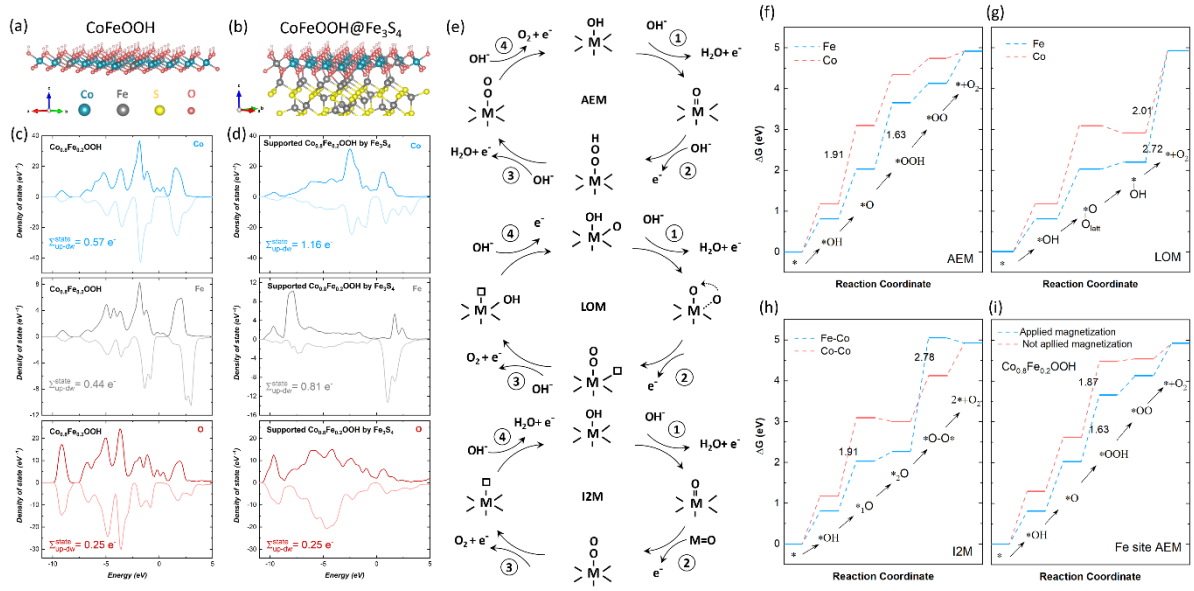

Figure 5. The DFT studies of interfacial configurations. a, b) The computational models of $Co_{0.8}Fe_{0.2}OOH$ (a) and $Co_{0.8}Fe_{0.2}OOH@Fe_3S_4$ interfacial configuration (b). c, d) The projected density of state (pDOS) of $Co_{0.8}Fe_{0.2}OOH$ without and with Fe_3S_4. All states of Fe_3S_4 have been excluded. e) The OER steps on $Co_{0.8}Fe_{0.2}OOH$ under AEM, LOM, and I2M mechanisms. f-h) The Gibbs free energy diagram for $Co_{0.8}Fe_{0.2}OOH$ with Co or Fe as active site under AEM (f), LOM (g), and I2M mechanism (h). i) The Gibbs free energy diagram for $Co_{0.8}Fe_{0.2}OOH$ with and without applied magnetizations of atoms same as that in $Co_{0.8}Fe_{0.2}OOH$ @ Fe_3S_4. The energetics are calculated for the AEM pathway at Fe site on $Co_{0.8}Fe_{0.2}OOH$.

To understand the energetics of OER steps on $Co_{0.8}Fe_{0.2}OOH$, we calculated the Gibbs free energy along with OER steps under the adsorbate evolution mechanism (AEM), lattice oxygen oxidation mechanism (LOM) and the interaction of two M-O entities mechanism (I2M) at both Co and Fe sites on $Co_{0.8}Fe_{0.2}OOH$. The magnetizations of atoms have been applied on $Co_{0.8}Fe_{0.2}OOH$ as same as that of $Co_{0.8}Fe_{0.2}OOH$ with Fe_3S_4. All reaction intermediates of $Co_{0.8}Fe_{0.2}OOH$ in AEM, LOM, and I2M are shown in Figure S11. The related OER steps on $Co_{0.8}Fe_{0.2}OOH$ under AEM, LOM, and I2M are described in Figure 5e. The Gibbs free energy diagrams along with the reaction coordinates are presented in Figure 5f-5h for AEM, LOM, and I2M pathways, respectively. The energetic barriers of potential-limited step (PLS) are denoted in all diagrams, where the lowest one (1.63 eV) is found for the AEM pathway at Fe site of $Co_{0.8}Fe_{0.2}OOH$, which agrees with recent finding about highly active Fe sites on $CoFeO_xH_y$.[34] Greater energetic barrier is found both for LOM and I2M. Under LOM, the deprotonation of -OH_{ads} to recover the lattice oxygen in $Co_{0.8}Fe_{0.2}OOH$ exhibit a great energetic barrier. Under I2M, the coupling of two M-O species is difficult, probably because of the long atomic distance between two ligand oxygens at metal sites (especially between the Fe and Co site) making a high energy barrier toward the M-O-O-M intermediate formation. At Co site, the high energy barrier of the deprotonation of ligand OH (1.91 eV) is a limitation under all three mechanisms. According to the DFT results, the AEM should be the preferred pathway on $Co_{0.8}Fe_{0.2}OOH$ and Fe site is more active than Co site in terms of energetics.

Furthermore, we studied the effect of the magnetic structure of $Co_{0.8}Fe_{0.2}OOH$ with and without Fe_3S_4 on the energetics of the AEM pathway at Fe site. The energetics were calculated on two $Co_{0.8}Fe_{0.2}OOH$ slabs, where one is applied with magnetizations of atoms as same as that of $Co_{0.8}Fe_{0.2}OOH$ with Fe_3S_4 (Figure 5i). Please see details in the Method part. For the AEM pathway at Fe site of $Co_{0.8}Fe_{0.2}OOH$, the O-O coupling process is the PLS and its energy barrier

is enlarged by 0.24 eV without applied magnetizations compared to that with applied magnetizations. The results indicate the critical contribution from the modification of the magnetic structure of $Co_{0.8}Fe_{0.2}OOH$ by Fe_3S_4. With the interface spin channel, the energetics of OER steps on $Co_{0.8}Fe_{0.2}OOH$ is further optimized to reduce the OER overpotential.

Coherent spin channels throughout the reconstructed $CoFe_2S_4$ are significant for the high intrinsic activity of OER, because OER involves spin-dependent kinetics and spin-polarized electron transfer.[9a, 9b] The OER starts with singlet reactants (OH^-, H_2O) to produce triplet oxygen (↑O=O↑). A high-performing catalyst will be able to realize spin conservation for fast OER kinetics, in which the intrinsic spin channels can facilitate spin polarization processes. Specifically, with spin channels in OER catalysts, the OER intermediates will adopt specific rather than arbitrary spin directions. This is usually achieved by spin-selective electron transfer which is supported by open-shell quantum spin exchange interaction between adsorbed species and catalysts.[35] When screening the oxygen ligands in OER intermediates, they can be with radical character as found in recent potential-dynamic XAS studies.[36] The spin direction of these oxygen radicals will be affected by spin channels, which is believed to be a key prerequisite for the O-O coupling with lower barrier. As O_2 has two π^* electrons in parallel alignment, substantial kinetic barriers can be resulted by the need of aligning the spins of two oxygens during the O-O coupling, making the O-O coupling a rate-determining step for OER.[32] But with spin channels to facilitate the generation of oxygen radicals in parallel spin alignment, the O-O coupling will encounter a lower barrier. It should also note that the O=O bond formation during OER is not restricted to the simple coupling of two oxygen radicals. For more complicated OER steps, the spin channels can still carry out spin-selective electron transfer to reduce the barrier for final O_2 turnover. The spin-sensitive OER pathways under AEM, LOM and I2M have been previously well discussed by us elsewhere.[37] Overall, spin

channels in reconstructed $CoFe_2S_4$ will provide an effective way to reduce the barrier of O-O coupling and promote the efficiency of O_2 turnover.

2.4. MEA performance of reconstructed $CoFe_2S_4$

In the derived $Co(Fe)O_xH_y$, the amorphous structure should adapt a lot of defects such as cation/anion vacancies, grain boundaries, etc, which can significantly increase the electrochemically-accessible active sites.[38] That may also contribute to a high activity,[39] which is usually believed as one of the advantages of pre-catalyst and with high practical interest.[40] For the practical application of pre-catalysts, the conductivity of the reconstructed species is also critical. In alkaline OER, the reconstruction is usually believed to generate (oxy)hydroxide species. However, the 3d transition metal (oxy)hydroxides are mostly insulating or semiconducting. A typical way to address this conductivity issue is by mixing these insulating catalysts with conductive agents such as carbon black during electrode fabrication.[41] In reconstructed $CoFe_2S_4$, the generated Fe_3S_4 has a half-metal property with intrinsic conductivity of ~ 0.1 S cm^{-1},[42] comparable to that of carbon black (acetylene black (Alfa), ~0.17 S cm^{-1}). The OER measurement was performed using the reconstructed $CoFe_2S_4$ with and without carbon support. The result (Figure S12) shows limited activity difference between the reconstructed $CoFe_2S_4$ with and without using carbon support. It implies that the conductivity issue of the reconstructed oxyhydroxides could be addressed by the Fe_3S_4 component in reconstructed $CoFe_2S_4$. The high performance of reconstructed $CoFe_2S_4$ that does not rely on the usage of carbon black is of great practical interest under MEA configuration.

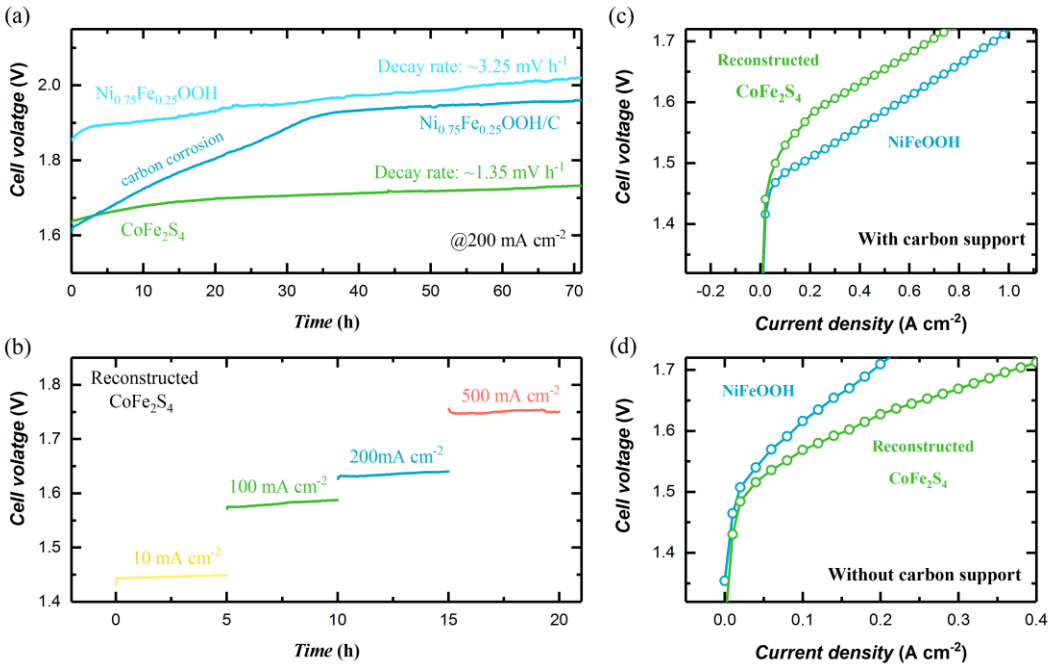

Figure 6. The application and performance of $CoFe_2S_4$ under MEA configuration. a) The chronopotentiometry of $Ni_{0.75}Fe_{0.25}OOH$ with and without carbon (denote as $Ni_{0.75}Fe_{0.25}OOH$ and $Ni_{0.75}Fe_{0.25}OOH$/C) and $CoFe_2S_4$ without carbon under a current density of 200 mA cm^{-2} for 70 hours in a membrane electrode assembly (MEA) cell. b) The chronopotentiometry of $CoFe_2S_4$ under current densities of 10, 100, 200, and 500 mA cm^{-2} in an MEA cell. c,d) The MEA performance by testing $Ni_{0.75}Fe_{0.25}OOH$ (4 mg cm^{-2}) and $CoFe_2S_4$ (4 mg cm^{-2}) with (b) and without (c) carbon support. Pt/C (TKK 47.1 wt% Pt, 1 mg cm^{-2}) was used as the cathode catalyst. The current density is obtained by normalizing the current to the effective area of current collectors. The cell temperature of all MEA measurements was maintained at 60 ^{o}C with an electrolyte flow of 10 ml min^{-1}.

Some directly-prepared oxyhydroxides were found state-of-art toward alkaline OER, in which the high intrinsic activity of $NiFeO_xH_y$ is very impressive.[21] However, the application of directly-prepared oxyhydroxides under MEA configuration is greatly hampered by the conductivity issue.[43] It should be noted that carbon-based conductive agents are not stable under the high voltage (or current) condition at the anode of MEA.[44] To demonstrate the difference between using the directly-prepared oxyhydroxide and the pre-catalyst under MEA configuration, the $CoFe_2S_4$ and $Ni_{0.75}Fe_{0.25}OOH$ were tested in a MEA electrolyzer with anion exchange membrane (Figure S13). A $Ni_{0.75}Fe_{0.25}OOH$ has been synthesized by a coprecipitation

method. The synthesis details and characterizations are given in Supplementary Note 1. The intrinsic activity of as-synthesized $Ni_{0.75}Fe_{0.25}OOH$ is comparable to the benchmark $Ni_{0.75}Fe_{0.25}O_xH_y$ NPs in terms of surface TOF (Figure 2a).

The $Ni_{0.75}Fe_{0.25}OOH$ with and without mixing carbon were tested by the chronopotentiometry method under a current density of 200 mA cm^{-2} in MEA for 70 hours (Figure 6a). The initial cell voltage with $Ni_{0.75}Fe_{0.25}OOH$/C anode is much lower than that with $Ni_{0.75}Fe_{0.25}OOH$ anode, which is consistent with the reported intrinsic conductivity issue of pure $Ni_{0.75}Fe_{0.25}OOH$.[43] The activity of the cell with $Ni_{0.75}Fe_{0.25}OOH$/C anode degrades greatly in the first 35 hours, which is due to the corrosion of carbon and thus raising the conductivity issue in MEA. Such a result implies that the conductivity issue of $Ni_{0.75}Fe_{0.25}OOH$ that limits the overall cell performance cannot be solved by using carbon. However, this issue in MEA application can be addressed by using the pre-catalyst $CoFe_2S_4$ because its distinguished reconstruction behaviours lead to excellent conductivity after reconstruction. The $CoFe_2S_4$ was also tested by the chronopotentiometry for 70 hours. Before the test, the $CoFe_2S_4$ had been cycled for 50 times in 1 M KOH to complete reconstruction. With a $CoFe_2S_4$ anode, the cell exhibits a much lower voltage than that with pure $Ni_{0.75}Fe_{0.25}OOH$ (slightly higher than the initial voltage with $Ni_{0.75}Fe_{0.25}OOH$/C anode). The cell also keeps a low decay rate of the cell performance throughout the measurement. The stability of $CoFe_2S_4$ under various current densities of 10, 100, 200, and 500 mA cm^{-2} is demonstrated in Figure 6b. Further, the activities of $CoFe_2S_4$ with and without carbon were examined by the polarization curve of the cell, compared with $Ni_{0.75}Fe_{0.25}OOH$ in Figure 6c and 6d. With carbon, $Ni_{0.75}Fe_{0.25}OOH$ outperforms reconstructed $CoFe_2S_4$ based on the polarization curves. However, without carbon, the cell performance with $Ni_{0.75}Fe_{0.25}OOH$ anode is greatly compromised. The reconstructed $CoFe_2S_4$ exhibits much higher activity than $Ni_{0.75}Fe_{0.25}OOH$ in the MEA cell. In addition, the activity of $CoFe_2S_4$ is also superior to IrO_2 (Figure S14). Considering that additive carbon is not applicable under the

tough working condition of the anode, the reconstructed $CoFe_2S_4$ can be a better choice than directly-prepared oxyhydroxides in MEA electrolyzers.

3. Conclusion

In summary, we have investigated a sulfide pre-catalyst $CoFe_2S_4$ and revealed its reconstruction chemistry. The reconstructability of $CoFe_2S_4$ is credited to the high (M-S) bonding state close to the LHB, which facilitates anionic redox and creates structural flexibility for reconstruction. In the reconstruction of $CoFe_2S_4$, Co and Fe behave differently: Co is more inclined to reconstruct into oxyhydroxide at the surface region, while Fe-S component is more stable in the bulk region in a major form of greigite Fe_3S_4. At the interface of Fe_3S_4/ $Co(Fe)O_xH_y$, the interface spins are pinned and follow the polarized spins in Fe_3S_4. The spin-polarized interfaces in reconstructed $CoFe_2S_4$ create a spin channel to optimize the energetics of OER steps and facilitate the spin-sensitive electron transfer in OER. It facilitates the spin polarization to produce oxygen molecules in its ground state and is thus responsible for a high intrinsic OER activity. With the Fe_3S_4 component, the high intrinsic activity of reconstructed $CoFe_2S_4$ can be maintained without using carbon support. This advantage enabled the application of $CoFe_2S_4$ in an MEA water electrolyzer without using carbon. The critical conductivity issue to maintain the high performance of oxyhydroxides without adding conductive support can be addressed with a pre-catalyst strategy. Overall, the distinguished reconstruction behaviour of $CoFe_2S_4$ demonstrates notable advantages of using pre-catalysts over directly prepared catalysts. The principles and mechanisms revealed in this work provide new insights into the pre-catalysts design for water oxidation. Applying high-performing pre-catalyst in MEA electrolyzers facilitates efficient hydrogen production, which is significant for sustainable development.

4. Experimental Methods

$CoFe_2S_4$ and $CoFe_2O_4$ synthesis: In the synthesis of $CoFe_2S_4$, $CoCl_2$ (1 mmol) and $FeCl_3$ (2 mmol) were dissolved in the 40 ml ethylene glycol (EG) and stirred at 80 °C for 2 hours. Then, thiourea (4 mmol) was added to the suspension, followed by stirring for another 1 hour. The obtained suspension was then transferred into an autoclave (100 ml). The solvothermal reaction was maintained at 200 °C for 12 hours in an oven. The synthesis of $CoFe_2O_4$ followed a sol-gel method as described elsewhere.[11] Cobalt acetate $(Co(OAc)_2{\cdot}4H_2O)$ and Iron(III) nitrate nonahydrate $(Fe(NO_3)_3 \cdot 9H_2O)$ were mixed in a molar ratio of 1:2, then dissolving in the diluted nitric acid. The Citric acid and urea were added into the solution followed by stirring and

heating at 80 °C to give finally a viscous gel. The viscous gel was dried and decomposed at 170 °C in an oven for 12 hours. The obtained samples were calcinated at 400 °C to give the crystalline product $CoFe_2O_4$.

Materials characterization: The X-ray diffraction (XRD) of $CoFe_2O_4$ and $CoFe_2S_4$ were performed on Bruker D8 diffractometer at a scanning rate of 2° min^{-1}, under Cu-K_α radiation (λ = 1.5418 Å). ICP-OES measurements were carried out on THERMO IRIS. The sample was dissolved in acid (HNO_3) and then were diluted with Milli-Q water to ensure the signal within appropriate emission intensity. The X-ray adsorption fine structure (XAFS) was performed under transmission mode at Singapore Synchrotron Light Source, XAFCA beamline and 8-BM beamline of National Synchrotron Light Source II . Acquired XAFS data were processed in ATHENA program and analysed in ARTEMIS program integrated with IFEFFIT software package.[45] The XPS measurements were carried on a PHI-5400 equipment with Al Kα beam source (250 W) where position-sensitive detector (PSD) was used to determine the composition of the materials. The DC magnetization measurements were performed on a Superconducting Quantum Design (SQUID) magnetometer (MPMS-XL). The cycled $CoFe_2S_4$ powder was accurately weighted before measurements. The SQUID measurements of the magnetization of cycled $CoFe_2S_4$ as a function of magnetic field were carried out at 300 K in fields between -5 T and +5 T. The high-resolution TEM (HRTEM) and STEM-EELs were carried out on a JEOL 2100 plus microscope at 200KV.

Electrodes preparation and electrochemical characterization: The working electrode was fabricated by drop casting method. The as-prepared catalysts which first mixed with acetylene black (AB) at a mass ratio of 5:1, then were dispersed in isopropanol/water (v/v=1:4) solvent followed by the addition of Na^+-exchanged Nafion as the binder and ultrasonicated for 30 min to form homogeneous ink. The electrodes were also prepared without adding acetylene black (AB) for performance comparison. The glassy carbon electrodes were polished to a mirror finish with 50 nm α-Al_2O_3 and ultrasonicated in IPA and water to completely clean up. At last, 10 μl of the as-prepared ink was dropped onto a glassy carbon (GC) electrode (0.196 cm^2) and dried overnight at room temperature to yield a final loading mass of 255 $\mu g_{ox}\, cm^{-2}$.

The electrochemical tests were carried out by three-electrode method using as-prepared catalysts on working electrode, platinum plate (1×2 cm^2) as the counter electrode, Hg/HgO (1M KOH, aqueous, MMO) as the reference. The electrodes systems were measured in O_2-saturated 1.0 M KOH by using Bio-logic SP 150 potentiostat. All potentials have been converted to RHE scale and iR corrected by a measured resistance of electrolyte. The conversion between the

potentials vs. RHE and vs. MMO was shown as follow: E (vs. RHE) = E (vs. MMO) + E_{MMO} (vs. SHE) + 0.059 × pH. E_{MMO} (vs. SHE) = 0.098 vs. SHE at 25°C. The Cyclic Voltammetry(CV) was obtained under potentials from 0.875V to 1.575V (vs. RHE) at a scan rate of 10mV s^{-1}. The TOF was obtained according to the equation:

$$TOF = \frac{j \times A}{4Fn}$$

Where j is the current density (A cm_{disk}^{-2}) delivered at an overpotential of 300 mV; A is the disk area of glassy carbon electrode (0.196 cm^{-2}), *F* is the Faraday constant (96485 C /mol); n is the number of active sites (mole). n is estimated by either assuming all active metal atoms in the catalyst are effective (denoted as "bulk") or calculating only the active metal atoms on the surface (denoted as "surface"). The TOF_{bulk} and $TOF_{surface}$ present the low and upper limits of the estimated TOF for fair comparison. The n_{bulk} of $CoFe_2S_4$ is estimated by assuming all Co in $CoFe_2S_4$ is active in oxyhydroxides. The $n_{surface}$ of $CoFe_2S_4$ is obtained by an average integral area of the Co^{2+}/Co^{3+} anodic and cathodic peaks (Figure S16), assuming an one-electron process.[20] The n_{bulk} of $Co_{0.86}Fe_{0.14}(OOH)$ is reported to be estimated according to the measurement of the catalyst mass and composition by *in-situ* QCM and *ex-situ* XPS.[17] The $n_{surface}$ is calculated by n_{bulk}/x%, where x% is the fraction of Co in deposited $Co_{0.86}Fe_{0.14}(OOH)$ that is electrochemically active (x%=27%, 2nd cycle).[17] The n_{bulk} of BSCF film is reported to be calculated according to the unit cell volume, film thickness, and electrode area.[46] The $n_{surface}$ is reported to be determined by calculating the number of atoms on an assumed (100) surface according to the refined lattice parameters and the surface area of oxides that is decided by Brunauer-Emmett-Teller (BET) measurement.[46] The $n_{surface}$ of "Co-Pi" is reported to be obtained by the surface density of "Co-Pi" from EXAFS characterization.[20, 46] The $n_{surface}$ of $Ni_{0.75}Fe_{0.25}O_xH_y$ is reported to be estimated by the integral of the Ni^{2+} to $Ni^{3+/4+}$ redox couple in CVs.[21] The n_{bulk} of BSCF, "Co-Pi", NiFe-LDH and Co_3S_4 are reported to be estimated by all active metal atoms in the catalysts loaded on the electrodes.

SQUID Measurement: DC magnetization measurements were performed on a Superconducting Quantum Design (SQUID) magnetometer (MPMS-XL). The samples were accurately weighted before measurements. For obtaining a typical magnetic hysteresis loop, the SQUID measured the magnetization of samples as a function of magnetic field between -5 T and +5 T. To measure the exchange bias of reconstructed $CoFe_2S_4$, the pristine $CoFe_2S_4$ was firstly cycled in 1 M KOH for ~ 20 cycles and dried under N_2. The cycled $CoFe_2S_4$ (1~2 mg) was then encapsulated and transferred to the chamber. Before SQUID measurement, all samples were completely demagnetized under oscillated field. The SQUID measurement under 2 K was then carried

under field-cooled (FC) mode and zero-field-cooled (ZFC) mode. Under FC mode, a field of 5 T was applied during cooling process from 300 K to 2 K, while under ZFC mode, the filed was zero. After cooling process, the M-H measurement of hysteresis loop was carried out.

Computational methods: All the density functional theory (DFT) calculations were performed by Vienna Ab-initio Simulation Package[47] (VASP), employing the Projected Augmented Wave[48] (PAW) method. The Perdew-Burke-Ernzerhof (RPBE) functional was used to describe the exchange and correlation effects.[49] For all the geometry optimizations, the cutoff energy was set to be 450 eV. The $Co_{0.8}Fe_{0.2}OOH$ model was constructed by using a 5×5 supercell, containing twenty cobalt atoms and five iron atoms. The (111) surface of Fe_3S_4 was chosen to serve as the support for $Co_{0.8}Fe_{0.2}OOH$. The Monkhorst-Pack grids[50] were set to be 2×1×1 to carry out the surface calculations on the layered $Co_{0.8}Fe_{0.2}OOH$ and $Co_{0.8}Fe_{0.2}OOH@Fe_3S_4$. At least 20 Å vacuum layer was applied in z-direction of the slab models, preventing the vertical interactions between slabs.

The computational hydrogen electrode (CHE) model[51] was used to calculate the free energies of OER. The free energy of the adsorbed species is defined as

$$\Delta G_{ads} = \Delta E_{ads} + \Delta E_{ZPE} - T\Delta S_{ads}$$

where ΔE_{ads} is the electronic adsorption energy, ΔE_{ZPE} is the zero point energy difference between adsorbed and gaseous species, and $T\Delta S_{ads}$ is the corresponding entropy difference between these two states. The electronic binding energy is referenced as ½ H_2 for each H atom, and (H_2O – H_2) for each O atom, plus the energy of the clean slab. The slab models for calculating the free energy along with reaction coordinates are shown in Figure S11. The magnetization of the $Co_{0.8}Fe_{0.2}OOH$ slab models was controlled by using the NUPDOWN parameter.

MEA water electrolysis measurements: A home-made water electrolysis setup was employed to evaluate the performance of home-made OER catalyst. The electrolysis setup includes two stainless steel end plates, on which a circular serpentine channel with an area of 4.00 cm^2 was machined. The polarization curves were measured with an electrochemical workstation (Solartron 1470E). The catalyst ink was prepared by mixing $CoFe_2S_4$ powder, high surface area carbon (HSAC, Ketjen black EC-600J, weight ratio of 1:1) (Optional), PTFE suspension (60 wt% PTFE dispersion in water from Chemours), isopropyl alcohol and water. The catalyst ink was ultrasonicated for 30 minutes at room temperature and manually brushed onto a nickel foam. The $CoFe_2S_4$ loading in the as-prepared electrode was 4 mg cm^{-2}. The $CoFe_2S_4$ electrodes were cycled in 1 M KOH for 10 cycles for a complete reconstruction before measuring the cell

performance. The cathode electrode was fabricated with the same procedure except that a catalyst ink consisting of 47.1 wt% Pt/C catalyst and PTFE suspension was manually spread onto a carbon paper. The Pt/C loading was 1 mg cm^{-2}. An anion exchange membrane (A901, 11 μm, Tokuyama, OH^- conductivity: 38 mS cm^{-1}, Ion-exchange capacity: 1.7 mmol g^{-1}) was employed as the membrane. To reduce the contact resistance, the membrane sandwiched by the anode electrode and cathode electrode was pressed at a pressure of 1 MPa for 5 minutes at room temperature. The commercial IrO_2 power (Premetek Co) with a mass loading of 1 mg cm^{-2} was employed as the benchmark. 1 M KOH was pumped into the electrode channels by a peristaltic pump at a constant flow rate of 10 ml min^{-1}. The cell temperature (60°C) was maintained by an electric heating plate and measured by a thermocouple placed near the anode and cathode current collectors.

Supporting Information

Supporting Information is available from the Wiley Online Library or from the author.

Acknowledgements

Authors thank the support from the Singapore Ministry of Education Tier 2 Grant (MOE-T2EP10220-0001) and the Singapore National Research Foundation under its Campus for Research Excellence and Technological Enterprise (CREATE) programme, through the Cambridge Center for Carbon Reduction in Chemical Technology (C4T) and eCO2EP programmes. Authors appreciate the Facility for Analysis, Characterisation, Testing and Simulation (FACTS) in Nanyang Technological University for materials characterizations. This research used 8-BM of the National Synchrotron Light Source II, a U.S. Department of Energy (DOE) Office of Science User Facility operated for the DOE Office of Science by Brookhaven National Laboratory under Contract No. DE-SC0012704.

Competing interests

The authors declare no competing financial interests.

Received: ((will be filled in by the editorial staff))
Revised: ((will be filled in by the editorial staff))
Published online: ((will be filled in by the editorial staff))

References

[1] Z. W. Seh, J. Kibsgaard, C. F. Dickens, I. Chorkendorff, J. K. Nørskov, T. F. Jaramillo, *Science* **2017**, 355, eaad4998.
[2] a)W. Chao, F. Zhenxing, S. G. G., B. James, S. H. Yang, X. Z. J., *Adv. Mater.* **2017**, 29, 1606800; b)J. Suntivich, K. J. May, H. A. Gasteiger, J. B. Goodenough, Y. Shao-Horn, *Science* **2011**, 334, 1383.
[3] a)A. Grimaud, C. E. Carlton, M. Risch, W. T. Hong, K. J. May, Y. Shao-Horn, *J. Phys. Chem. C* **2013**, 117, 25926; b)M. Risch, A. Grimaud, K. J. May, K. A. Stoerzinger, T. J. Chen, A. N. Mansour, Y. Shao-Horn, *J. Phys. Chem. C* **2013**, 117, 8628; c)A. Grimaud, *Nat. Catal.* **2018**, 1, 242.
[4] a)M. Görlin, J. Ferreira de Araújo, H. Schmies, D. Bernsmeier, S. Dresp, M. Gliech, Z. Jusys, P. Chernev, R. Kraehnert, H. Dau, P. Strasser, *J. Am. Chem. Soc.* **2017**, 139, 2070; b)C. Yang, O. Fontaine, J. M. Tarascon, A. Grimaud, *Angew. Chem. Int. Ed.* **2017**, 56, 8652.
[5] A. Bergmann, E. Martinez-Moreno, D. Teschner, P. Chernev, M. Gliech, J. F. de Araujo, T. Reier, H. Dau, P. Strasser, *Nat. Commun.* **2015**, 6, 8625.
[6] a)Z. J. Xu, *Sci. China Mater.* **2019**; b)C. Dette, M. R. Hurst, J. Deng, M. R. Nellist, S. W. Boettcher, *ACS Appl. Mater. Interfaces* **2019**, 11, 5590; c)J. Liu, J. Xiao, Z. Wang, H. Yuan, Z. Lu, B. Luo, E. Tian, G. I. N. Waterhouse, *ACS Catal.* **2021**, 11, 5386.
[7] a)Z.-F. Huang, J. Song, Y. Du, S. Xi, S. Dou, J. M. V. Nsanzimana, C. Wang, Z. J. Xu, X. Wang, *Nat. Energy* **2019**, 4, 329; b)H. Jiang, Q. He, Y. Zhang, L. Song, *Acc. Chem. Res.* **2018**, 51, 2968; c)B. R. Wygant, A. H. Poterek, J. N. Burrow, C. B. Mullins, *ACS Appl. Mater. Interfaces* **2020**, 12, 20366.
[8] E. Fabbri, M. Nachtegaal, T. Binninger, X. Cheng, B. J. Kim, J. Durst, F. Bozza, T. Graule, R. Schaublin, L. Wiles, M. Pertoso, N. Danilovic, K. E. Ayers, T. J. Schmidt, *Nat. Mater.* **2017**, 16, 925.
[9] a)J. Gracia, *Phys. Chem. Chem. Phys.* **2017**, 19, 20451; b)W. Mtangi, F. Tassinari, K. Vankayala, A. Vargas Jentzsch, B. Adelizzi, A. R. A. Palmans, C. Fontanesi, E. W. Meijer, R. Naaman, *J. Am. Chem. Soc.* **2017**, 139, 2794; c)E. Torun, C. M. Fang, G. A. de Wijs, R. A. de Groot, *J. Phys. Chem. C* **2013**, 117, 6353; d)X. Ren, T. Wu, Y. Sun, Y. Li, G. Xian, X. Liu, C. Shen, J. Gracia, H.-J. Gao, H. Yang, Z. J. Xu, *Nat. Commun.* **2021**, 12, 2608.
[10] R. R. Rao, M. J. Kolb, L. Giordano, A. F. Pedersen, Y. Katayama, J. Hwang, A. Mehta, H. You, J. R. Lunger, H. Zhou, N. B. Halck, T. Vegge, I. Chorkendorff, I. E. L. Stephens, Y. Shao-Horn, *Nat. Catal.* **2020**, 3, 516.
[11] T. Wu, S. Sun, J. Song, S. Xi, Y. Du, B. Chen, W. A. Sasangka, H. Liao, C. L. Gan, G. G. Scherer, L. Zeng, H. Wang, H. Li, A. Grimaud, Z. J. Xu, *Nat. Catal.* **2019**, 2, 763.
[12] Y.-L. Lee, J. Kleis, J. Rossmeisl, Y. Shao-Horn, D. Morgan, *Energy Environ. Sci.* **2011**, 4, 3966.
[13] Y. Duan, S. Sun, Y. Sun, S. Xi, X. Chi, Q. Zhang, X. Ren, J. Wang, S. J. H. Ong, Y. Du, L. Gu, A. Grimaud, Z. J. Xu, *Adv. Mater.* **2019**, 31, 1807898.
[14] G. Assat, J.-M. Tarascon, *Nat. Energy* **2018**, 3, 373.
[15] Y. H. Hou, Y. J. Zhao, Z. W. Liu, H. Y. Yu, X. C. Zhong, W. Q. Qiu, D. C. Zeng, L. S. Wen, *J. Phys. D: Appl. Phys.* **2010**, 43, 445003.
[16] M. Bajdich, M. García-Mota, A. Vojvodic, J. K. Nørskov, A. T. Bell, *J. Am. Chem. Soc.* **2013**, 135, 13521.
[17] M. S. Burke, M. G. Kast, L. Trotochaud, A. M. Smith, S. W. Boettcher, *J. Am. Chem. Soc.* **2015**, 137, 3638.
[18] a)M. Chauhan, K. P. Reddy, C. S. Gopinath, S. Deka, *ACS Catal.* **2017**, 7, 5871; b)Y. Liu, X. Xie, G. Zhu, Y. Mao, Y. Yu, S. Ju, X. Shen, H. Pang, *J. Mater. Chem. A* **2019**, 7, 15851.
[19] M. Risch, K. A. Stoerzinger, S. Maruyama, W. T. Hong, I. Takeuchi, Y. Shao-Horn, *J. Am. Chem. Soc.* **2014**, 136, 5229.

[20] Y. Surendranath, M. W. Kanan, D. G. Nocera, *J. Am. Chem. Soc.* **2010**, 132, 16501.
[21] C. Roy, B. Sebok, S. B. Scott, E. M. Fiordaliso, J. E. Sørensen, A. Bodin, D. B. Trimarco, C. D. Damsgaard, P. C. K. Vesborg, O. Hansen, I. E. L. Stephens, J. Kibsgaard, I. Chorkendorff, *Nat. Catal.* **2018**, 1, 820.
[22] a)H. Liao, T. Luo, P. Tan, K. Chen, L. Lu, Y. Liu, M. Liu, J. Pan, *Adv. Funct. Mater.* **2021**, 31, 2102772; b)T. Wang, G. Nam, Y. Jin, X. Wang, P. Ren, M. G. Kim, J. Liang, X. Wen, H. Jang, J. Han, Y. Huang, Q. Li, J. Cho, *Adv. Mater.* **2018**, 30, 1800757; c)L. Yu, L. Wu, B. McElhenny, S. Song, D. Luo, F. Zhang, Y. Yu, S. Chen, Z. Ren, *Energy Environ. Sci.* **2020**, 13, 3439.
[23] F. Song, X. Hu, *Nat. Commun.* **2014**, 5, 4477.
[24] X. Ren, C. Wei, Y. Sun, X. Liu, F. Meng, X. Meng, S. Sun, S. Xi, Y. Du, Z. Bi, G. Shang, A. C. Fisher, L. Gu, Z. J. Xu, *Adv. Mater.* **2020**, 32, 2001292.
[25] S. Liang, M. Jing, E. Pervaiz, H. Guo, T. Thomas, W. Song, J. Xu, A. Saad, J. Wang, H. Shen, J. Liu, M. Yang, *ACS Appl. Mater. Interfaces* **2020**, 12, 41464.
[26] C. Sugiura, *The Journal of Chemical Physics* **1984**, 80, 1047.
[27] E. M. Moon, R. T. Bush, D. H. M. Gibbs, J. P. Mata, *Chem. Geol.* **2017**, 468, 42.
[28] a)S. Yamaguchi, H. Wada, *J. Appl. Phys.* **1973**, 44, 1929; b)C.-S. Horng, A. P. Roberts, Y.-H. Chen, K.-S. Shea, K.-H. Chen, C.-H. Lin, X. Zhao, C.-K. Chang, *J. Geophys. Res.: Solid Earth* **2020**, 125, e2019JB018812.
[29] J. Sort, J. Nogués, X. Amils, S. Suriñach, J. S. Muñoz, M. D. Baró, *Appl. Phys. Lett.* **1999**, 75, 3177.
[30] D. Rickard, G. W. Luther, *Chem. Rev.* **2007**, 107, 514.
[31] H. Y. He, J. Fei, J. Lu, *Micro Nanosyst.* **2014**, 6, 126.
[32] T. Wu, X. Ren, Y. Sun, S. Sun, G. Xian, G. G. Scherer, A. C. Fisher, D. Mandler, J. W. Ager, A. Grimaud, J. Wang, C. Shen, H. Yang, J. Gracia, H.-J. Gao, Z. J. Xu, *Nat. Commun.* **2021**, 12, 3634.
[33] a)K. Haneda, A. Morrish, *IEEE Trans. Magn.* **1980**, 16, 50; b)A. H. Morr, K. Haneda, *J. Appl. Phys.* **1981**, 52, 2496.
[34] S. Lee, A. Moysiadou, Y.-C. Chu, H. M. Chen, X. Hu, *Energy Environ. Sci.* **2022**, 15, 206.
[35] J. Gracia, *J. Phys. Chem. C* **2019**, 123, 9967.
[36] a)O. Diaz-Morales, D. Ferrus-Suspedra, M. T. M. Koper, *Chemical Science* **2016**, 7, 2639; b)H. N. Nong, L. J. Falling, A. Bergmann, M. Klingenhof, H. P. Tran, C. Spöri, R. Mom, J. Timoshenko, G. Zichittella, A. Knop-Gericke, S. Piccinin, J. Pérez-Ramírez, B. R. Cuenya, R. Schlögl, P. Strasser, D. Teschner, T. E. Jones, *Nature* **2020**, 587, 408.
[37] T. Wu, Z. J. Xu, *Curr. Opin. Electrochem.* **2021**, 30, 100804.
[38] a)X. Liu, J. Meng, J. Zhu, M. Huang, B. Wen, R. Guo, L. Mai, *Adv. Mater.* **2021**, 33, 2007344; b)D. Cao, H. Shou, S. Chen, L. Song, *Curr. Opin. Electrochem.* **2021**, 30, 100788; c)Y. Chen, Z. Ren, H. Fu, X. Zhang, G. Tian, H. Fu, *Small* **2018**, 14, 1800763.
[39] T. Wu, M.-Y. Han, Z. J. Xu, *ACS Nano* **2022**, 16, 8531.
[40] J. N. Hausmann, P. W. Menezes, *Curr. Opin. Electrochem.* **2022**, 34, 100991.
[41] K. Hübner, G. Leonhardt, *Phys. Status Solidi B* **1975**, 68, K175.
[42] M. R. Spender, J. M. D. Coey, A. H. Morrish, *Can. J. Phys.* **1972**, 50, 2313.
[43] D. Xu, M. B. Stevens, M. R. Cosby, S. Z. Oener, A. M. Smith, L. J. Enman, K. E. Ayers, C. B. Capuano, J. N. Renner, N. Danilovic, Y. Li, H. Wang, Q. Zhang, S. W. Boettcher, *ACS Catal.* **2019**, 9, 7.
[44] S. Maass, F. Finsterwalder, G. Frank, R. Hartmann, C. Merten, *J. Power Sources* **2008**, 176, 444.
[45] M. Newville, *J. Synchrotron Radiat.* **2001**, 8, 322.
[46] W. T. Hong, M. Risch, K. A. Stoerzinger, A. Grimaud, J. Suntivich, Y. Shao-Horn, *Energy Environ. Sci.* **2015**, 8, 1404.

[47] a)G. Kresse, J. Furthmüller, *Phys. Rev. B* **1996**, 54, 11169; b)G. Kresse, J. Hafner, *Phys. Rev. B* **1994**, 49, 14251.
[48] P. E. Blöchl, *Phys. Rev. B* **1994**, 50, 17953.
[49] J. P. Perdew, K. Burke, M. Ernzerhof, *Phys. Rev. Lett.* **1996**, 77, 3865.
[50] H. J. Monkhorst, J. D. Pack, *Phys. Rev. B* **1976**, 13, 5188.
[51] J. K. Nørskov, J. Rossmeisl, A. Logadottir, L. Lindqvist, J. R. Kitchin, T. Bligaard, H. Jónsson, *J. Phys. Chem. B* **2004**, 108, 17886.

The electrochemical reconstruction of thiospinel $CoFe_2S_4$ evolves both oxyhydroxide species as active site and Fe_3S_4 component as spin channel, which is unique. The reconstructed $CoFe_2S_4$ shows state-of-art OER activity because of a strong magnetic anisotropy at the interface between oxyhydroxide and Fe_3S_4 components. The reconstructed configuration also benefits a robust performance in membrane electrolyzers.

Tianze Wu, Yuanmiao Sun, Xiao Ren, Jiarui Wang, Jiajia Song, Yangdan Pan, Yongbiao Mu, Jianshuo Zhang, Qiuzhen Cheng, Guoyu Xian, Shibo Xi, Chengmin Shen, Hong-Jun Gao, Adrian C. Fisher, Matthew P. Sherburne, Yonghua Du, Günther G. Schere, Joel W. Ager, Jose Gracia, Haitao Yang, Lin Zeng, Zhichuan J. Xu**

Reconstruction of thiospinel to active sites and spin channels for water oxidation

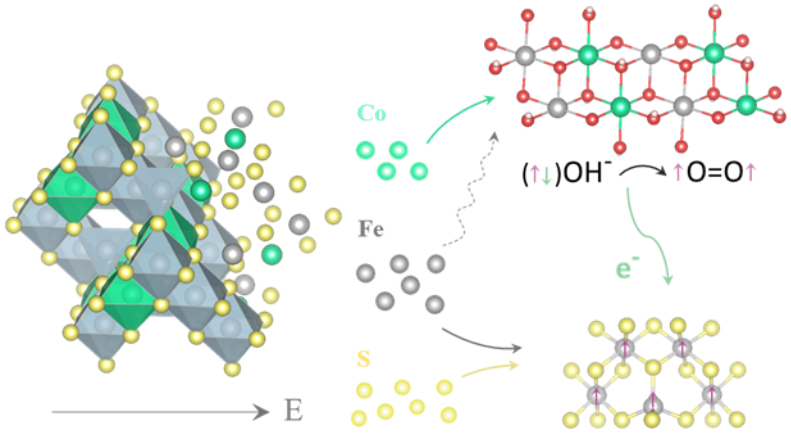

Supporting Information

Reconstruction of thiospinel to active sites and spin channels for water oxidation

Tianze Wu, Yuanmiao Sun, Xiao Ren, Jiarui Wang, Jiajia Song, Yangdan Pan, Yongbiao Mu, Jianshuo Zhang, Qiuzhen Cheng, Guoyu Xian, Shibo Xi, Chengmin Shen, Hong-Jun Gao, Adrian C. Fisher, Matthew P. Sherburne, Yonghua Du, Günther G. Schere, Joel W. Ager, Jose Gracia, Haitao Yang, Lin Zeng, Zhichuan J. Xu**

Supplementary Note 1. The $Ni_{0.75}Fe_{0.25}OOH$ were prepared by a coprecipitation method using 0.1 M solutions of $Ni(NO_3)_2$ and $Fe(NO_3)_3$ as precursors. The precipitation was performed at 80 °C. 10 mL water was first added to 0.1 M Na_2CO_3 solution (pH of 9.0). A solution containing 0.3 M $Ni(NO_3)_2$ and 0.1 M $Fe(NO_3)_3$ was then slowly added into the previously prepared solution. The pH was kept approximately constant at 9.0 during the synthesis by simultaneous dropping 0.1 M Na_2CO_3. The addition of the Ni^{2+}/Fe^{3+} solution (30 ml) and the Na_2CO_3 was completed within 1.5 h, after which the suspension was centrifugalized at 5000 rpm for 5mins. The powders were subsequently dried at 120 °C for 2 days. The XRD diffraction peaks of as-prepared $Ni_{0.75}Fe_{0.25}OOH$ (Figure S15) is consistent with the reported pattern in Ref 1.[1]

Supplementary Note 2. The greigite Fe_3S_4 synthesized by a hydrothermal method. $FeCl_3$ (4 mmol) and thiourea (8 mmol) were dissolved in 80 ml ethanol + water (3:1) solvent. The carmine solution was transferred into a 100 ml Teflon-lined stainless-steel autoclave. The autoclave was then kept in oven at 180 °C for 12 hours. The powder is obtained by centrifugation and washed by water and ethanol for 3 times. Black greigite Fe_3S_4 powder was then dried under vacuum at 60 °C for 6 hours. The powder XRD pattern of as-prepared Fe_3S_4 is shown in Figure S17. All diffraction peaks well match with cubic Fe_3S_4 (JCPDS 89-1998) phase.

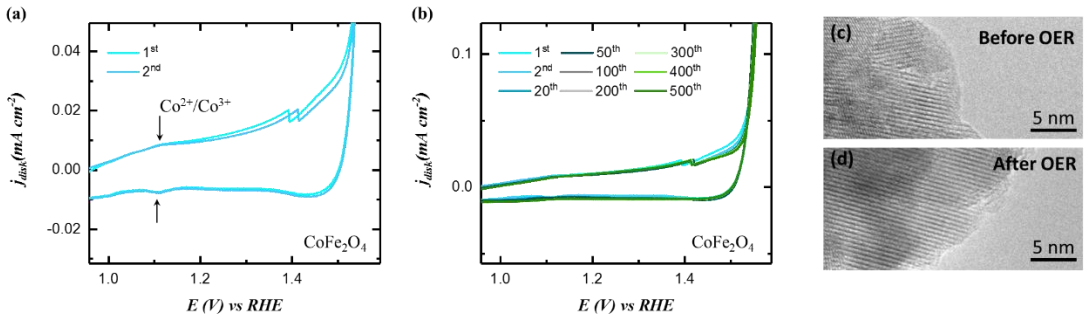

Figure S1. (a) The pseudocapacitive behavior in the 1st and 2nd CV cycle of $CoFe_2O_4$. A signal drop at ~ 1.4 V is because the potentiostat was changing caliber. (b) The 500 CV cycles of $CoFe_2O_4$ of 10 mV s^{-1} in 1 M KOH. (c-d) The HRTEM images of $CoFe_2O_4$ (c) before and (d) after 500 CV cycles.

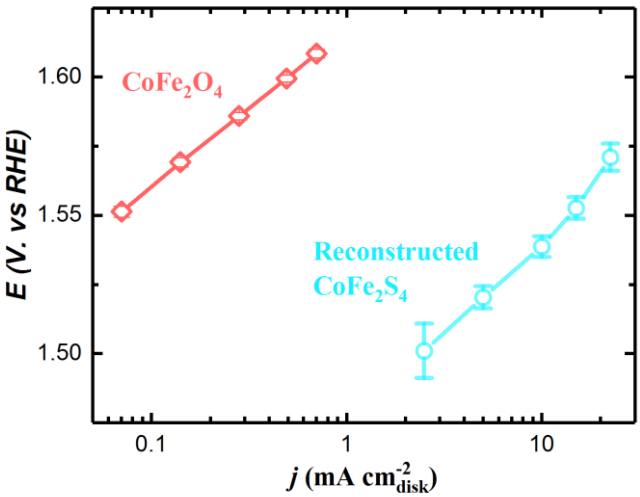

Figure S2. The Tafel plots of the reconstructed $CoFe_2S_4$ and $CoFe_2O_4$. The error bars represent the standard deviation from three independent measurements.

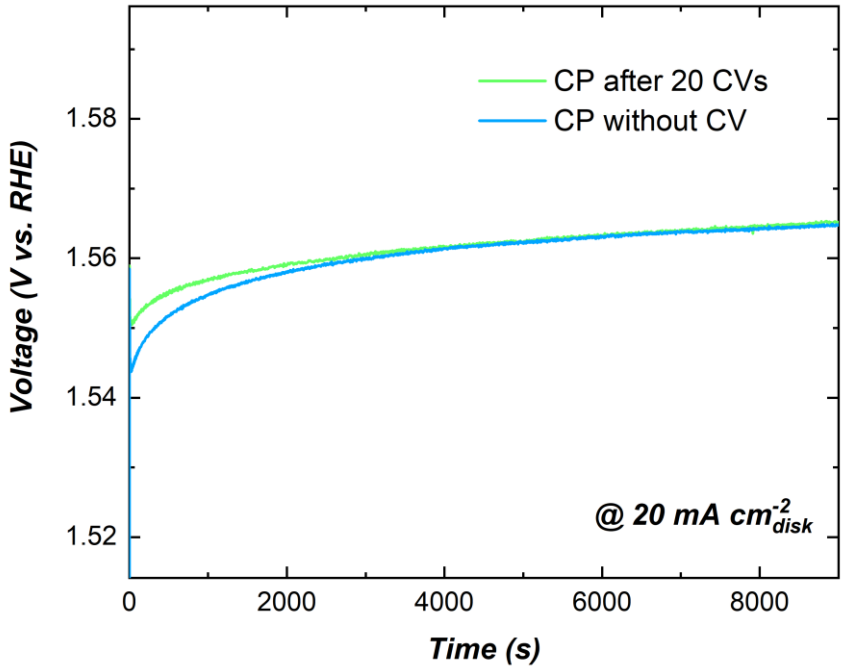

Figure S3. The measurements of chronopotentiometry (CP) after 20 CVs and CP without CV treatment in O_2-saturated 1 M KOH at a current density of 20 mA cm^{-2}. The cell voltages in these two cases are slightly different at the beginning but become nearly overlapped after ~ 2500 s.

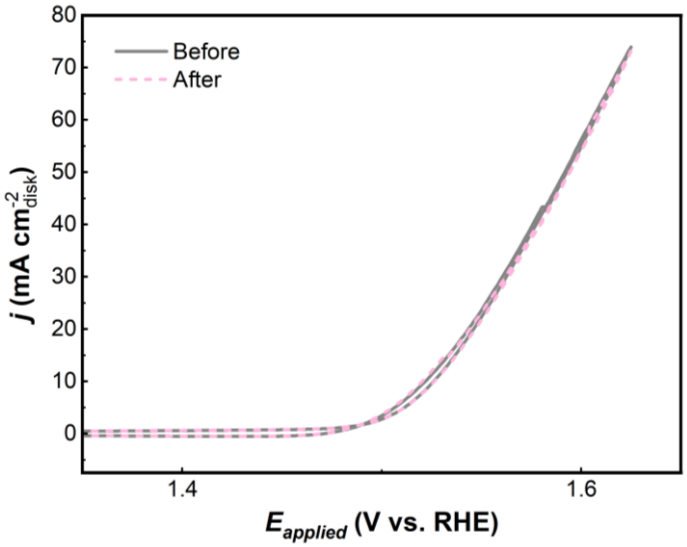

Figure S4. The OER CV of reconstructed $CoFe_2S_4$ before and after the cleaning of adsorbed SO_4^{2-}. To clean the surface of the catalyst, the electrode was rinsed by fresh electrolyte (O_2-saturated 1 M KOH) for three times and tested in fresh electrolyte.

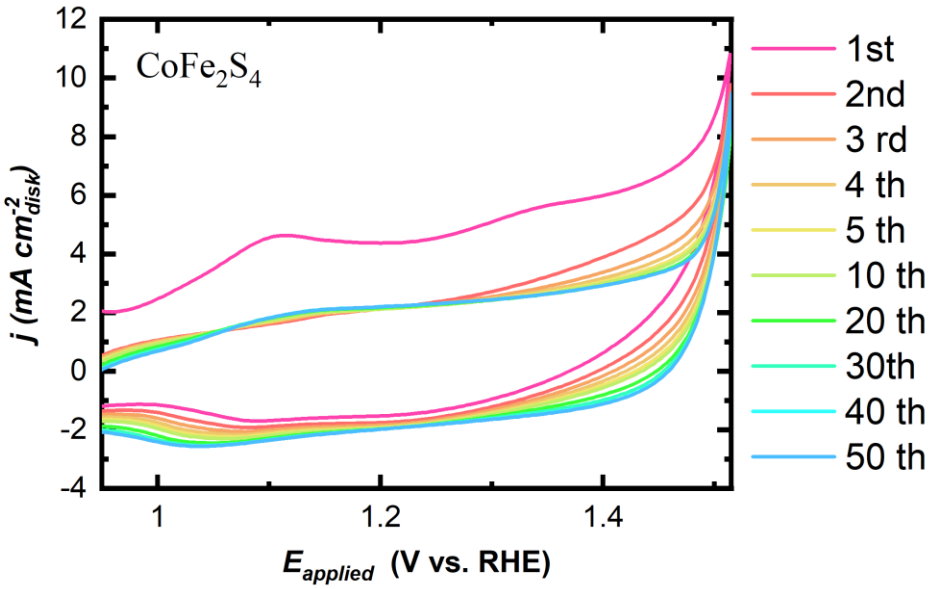

Figure S5. The pseudocapacitive behavior in 50 cycles of $CoFe_2S_4$ (coated on carbon paper) in 1 M KOH at a scan rate of 10 mV s^{-1} within a potential window between 0.90 and 1.55 V vs. RHE.

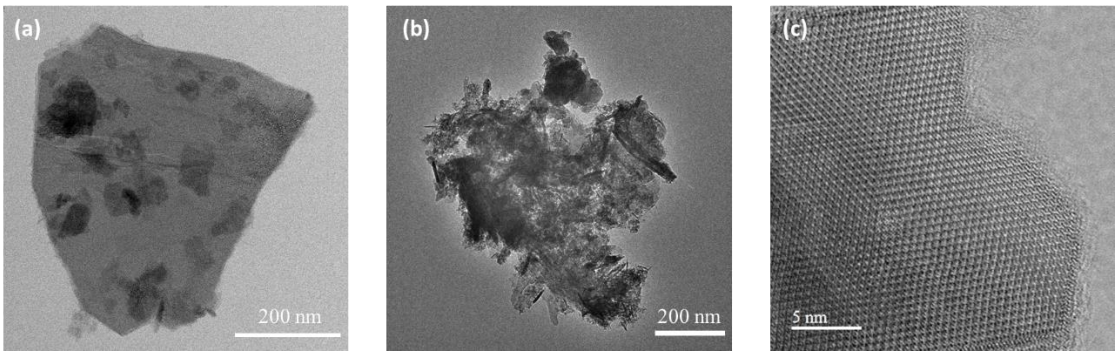

Figure S6. The TEM images of $CoFe_2S_4$ before (a) and after (b) OER cycling in 1 M KOH for 50 cycles. (c) The HRTEM of $CoFe_2S_4$ after immersed in O_2-satured 1.0 M KOH for 1 hour (around the same time as in our single activity measurement with about 20 CV cycles).

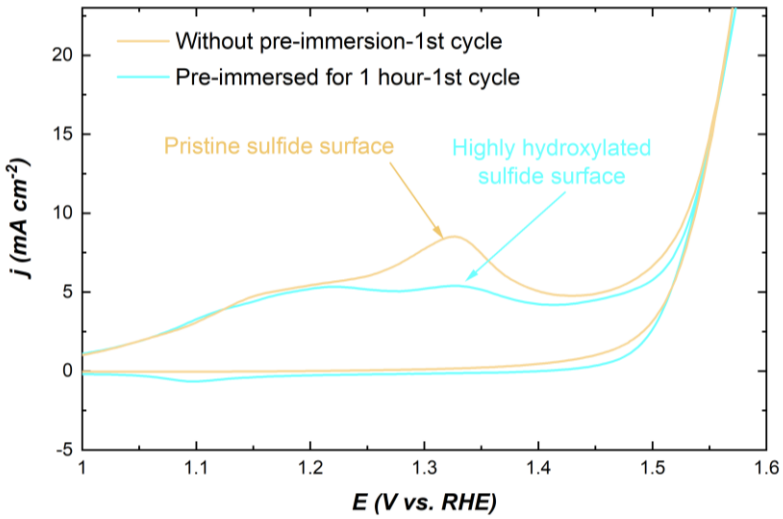

Figure S7. The OER CV (1st cycle) of $CoFe_2S_4$ with and without pre-immersion in O_2-saturated 1 M KOH for 1 hour.

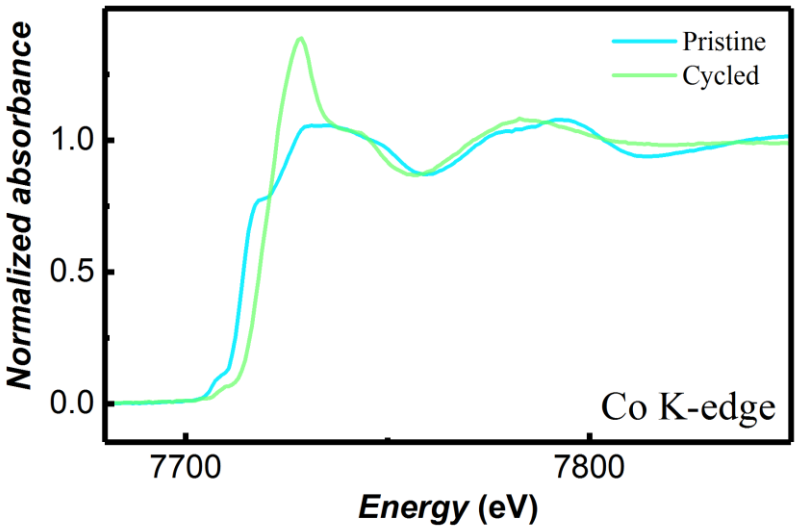

Figure S8. The normalized Co K-edge XANES spectra of $CoFe_2S_4$ before and after cycling.

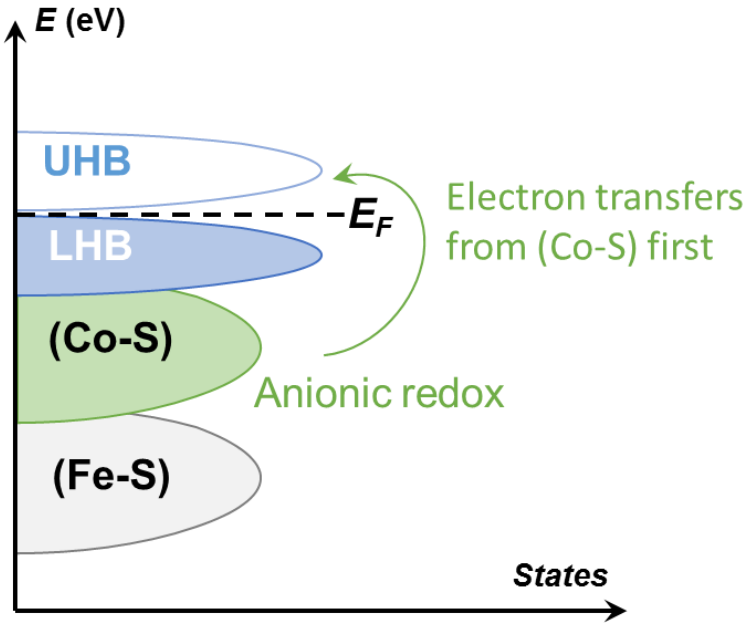

Figure S9. The schematic energy bands of $CoFe_2S_4$. The (Co-S) bonding states are closer to the LHB than (Fe-S) bonding states because the Co d band center is higher than Fe d band center in energy.

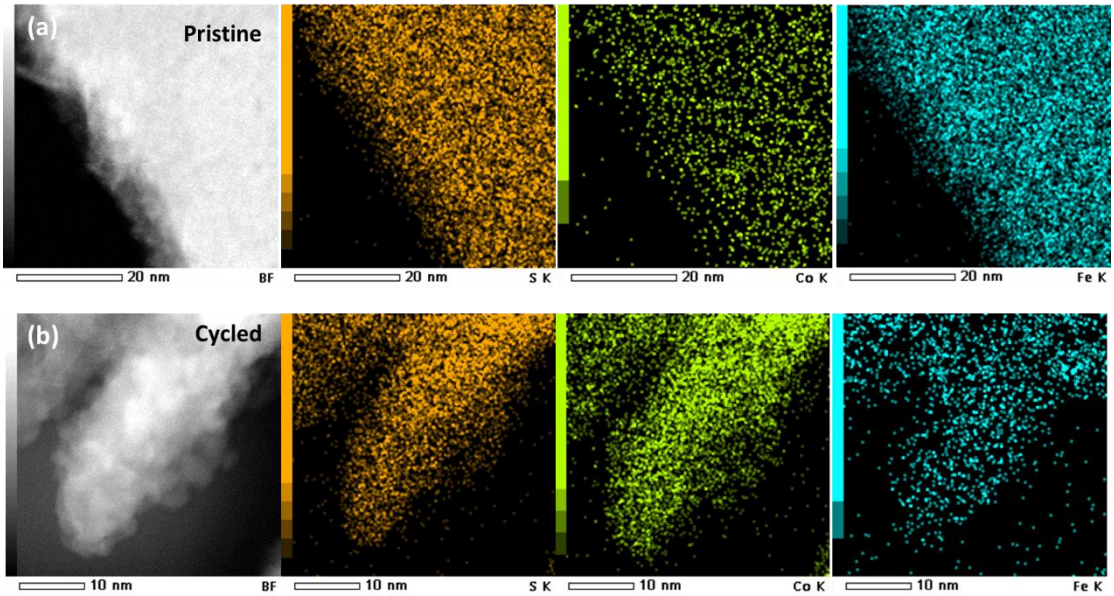

Figure S10. The EDX elemental mapping of Co, Fe, and S in $CoFe_2S_4$ before (a) and after (b) OER cycling in 1 M KOH for 50 cycles.

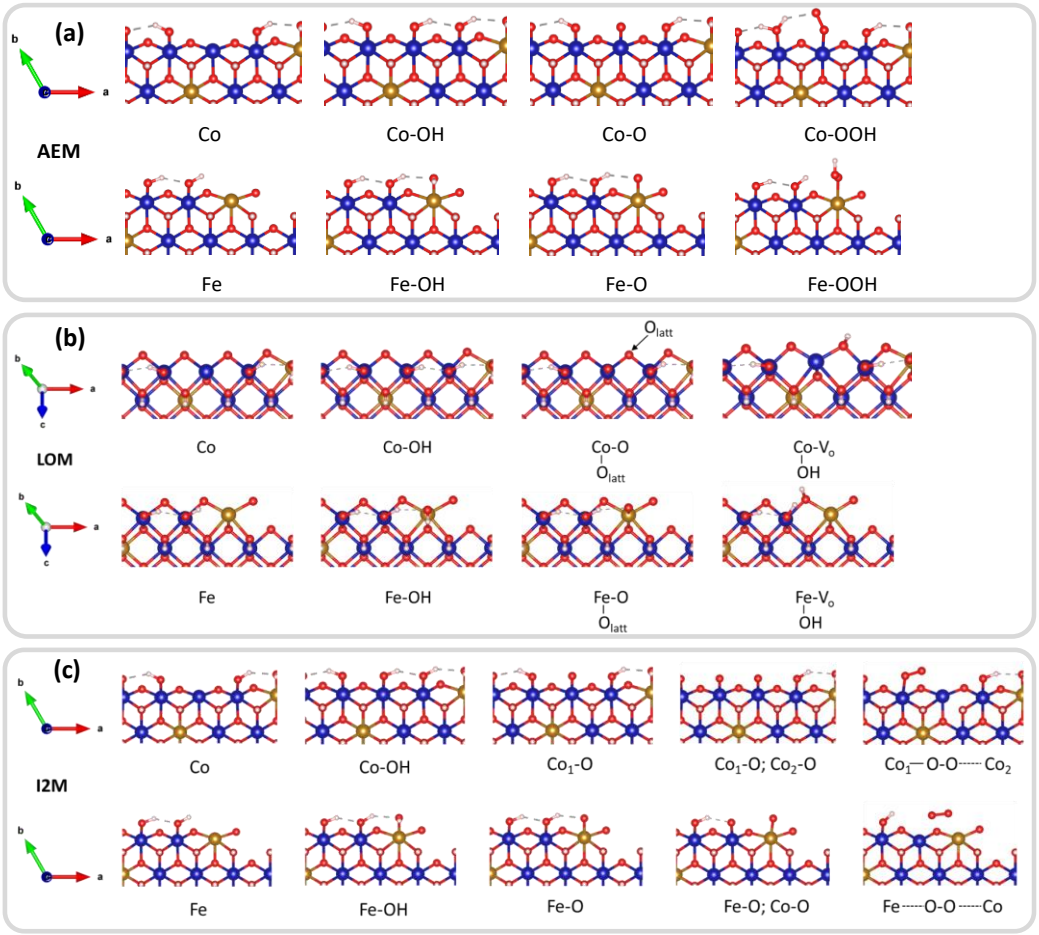

Figure S11. The reaction intermediates on $Co_{0.8}Fe_{0.2}OOH$ under (a) AEM, (b) LOM, and (c) I2M mechanisms with both Co and Fe as active site.

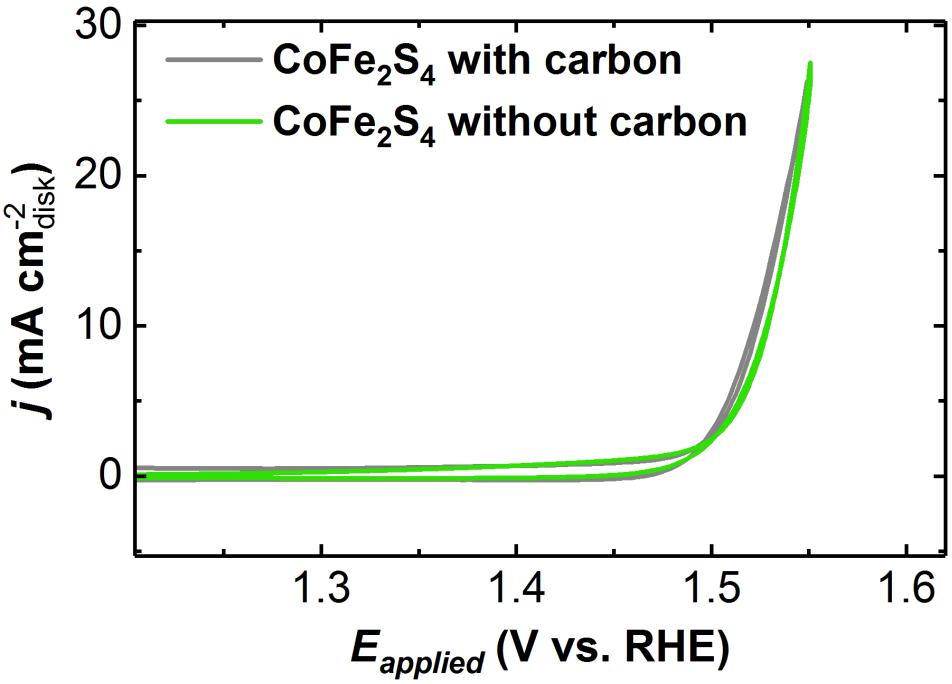

Figure S12. The CV curve (2nd cycle) of $CoFe_2S_4$ with and without mixing carbon (acetylene black).

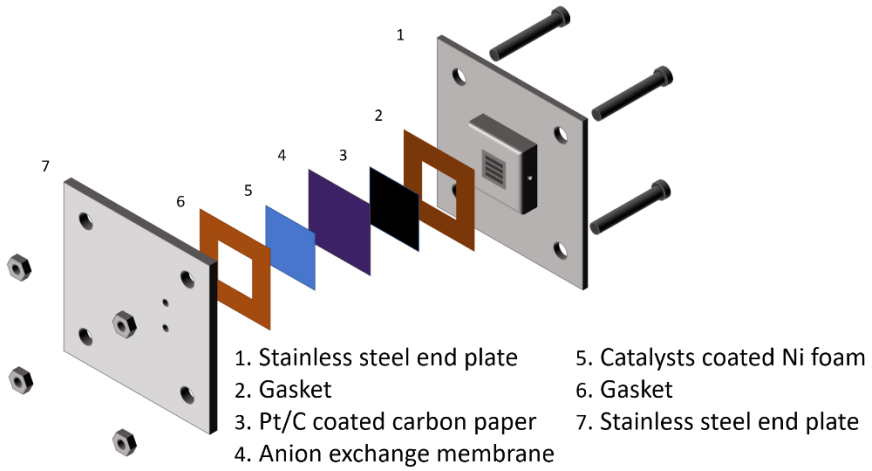

Figure S13. The schematics for membrane electrode assembly setup for measuring the cell performance of OER catalysts.

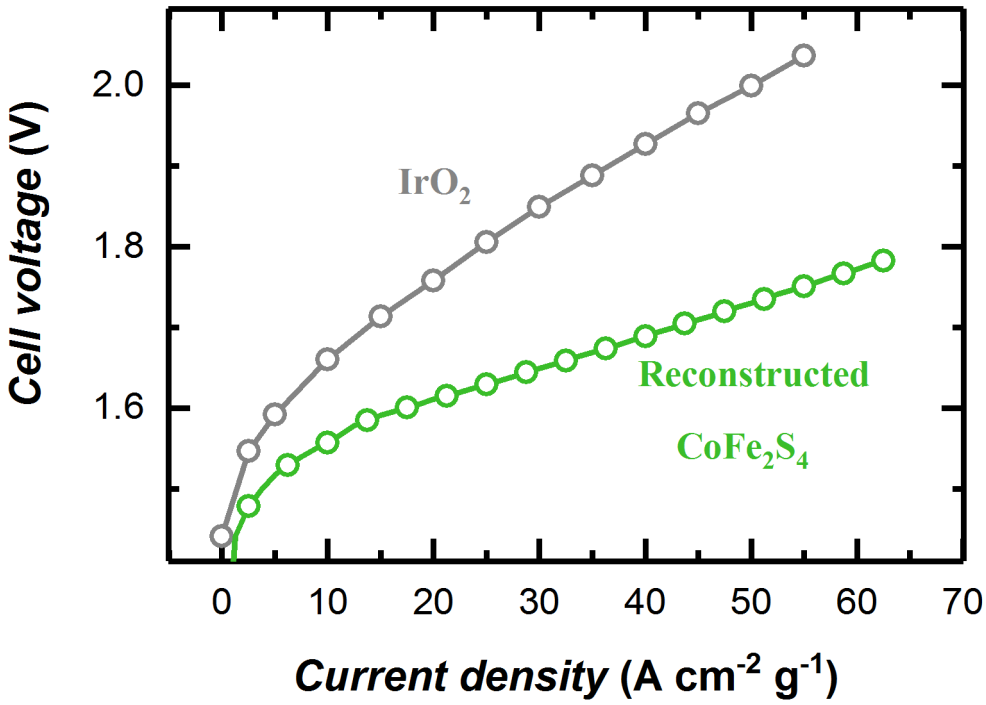

Figure S14. The MEA performance with $CoFe_2S_4$ and IrO_2 anodes without mixing with carbon. The cell temperature of MEA measurements was maintained at 60 ºC.

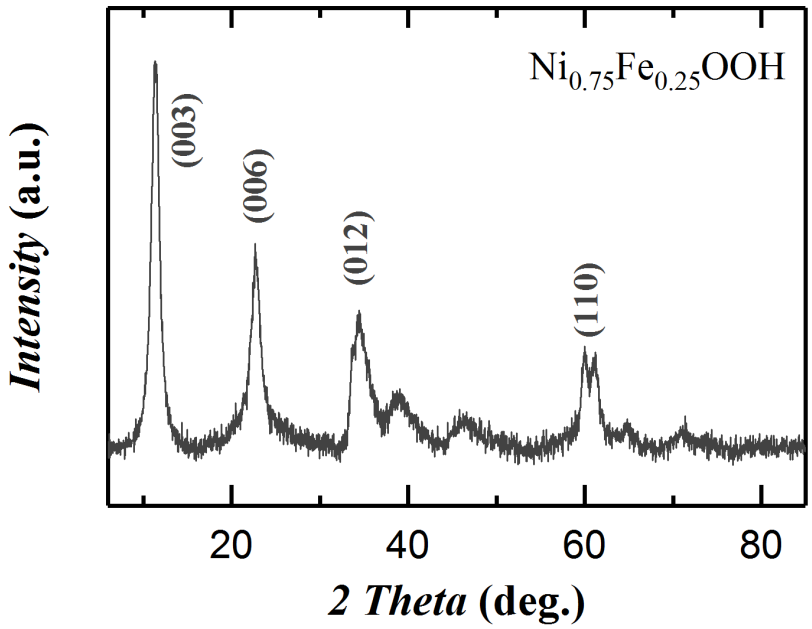

Figure S15. The powder X-ray diffraction (XRD) patterns of as-prepared $Ni_{0.75}Fe_{0.25}OOH$. The diffraction peaks are consistent with the reported pattern in the Ref 1.[1]

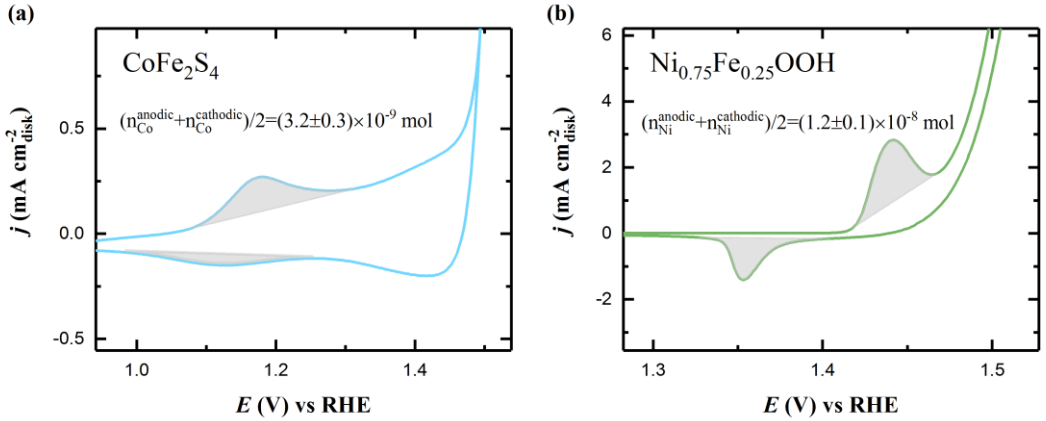

Figure S16. The Co^{2+}/Co^{3+} and $Ni^{2+}/Ni^{3+,4+}$ anodic and cathodic peaks in the steady CVs of (a) $CoFe_2S_4$ and (b) $Ni_{0.75}Fe_{0.25}OOH$, respectively. The N_{Co} and N_{Ni} are estimated by assuming a one-electron process.[2]

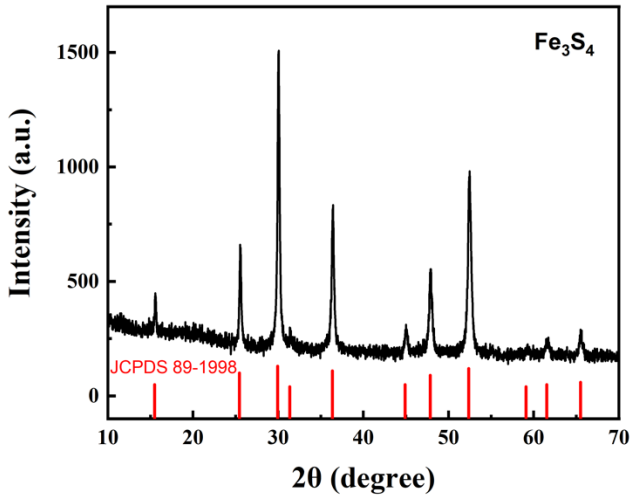

Figure S17. The powder XRD pattern of as-prepared Fe3S4.

Table S1. The results of DFT study of $CoFe_2S_4$ and $CoFe_2O_4$

	O 2p (eV)	Co 3d (eV)	Fe 3d (eV)	|Co 3d-O 2p| (eV)	|Fe 3d-O 2p| (eV)
$CoFe_2O_4$	-3.06	-1.57	-2.69	1.49	0.37
	S 3p (eV)	Co 3d (eV)	Fe 3d (eV)	|Co 3d-S 3p| (eV)	|Fe 3d-S 3p| (eV)
$CoFe_2S_4$	-2.55	-1.49	-2.85	1.06	0.3

Table S2. The baber charge analysis of Fe_3S_4

	CHARGE	MIN DIST	ATOMIC VOL	MAGNETIZATION
Fe1	6.605619	0.857079	12.117685	3.938
Fe2	6.605462	0.856888	12.115166	3.938
Fe3	6.598834	0.854575	12.016081	3.937
Fe4	6.598628	0.854595	12.0186	3.937
Fe5	6.597783	0.855229	11.999287	3.936
Fe6	6.598034	0.855248	11.999287	3.936
Fe7	6.598814	0.855127	12.02112	3.937
Fe8	6.59857	0.854968	12.016921	3.937
Fe9	6.779596	1.037168	11.027757	3.655
Fe10	6.800942	1.035938	10.764931	3.624
Fe11	6.801112	1.036016	10.765771	3.624
Fe12	6.800178	1.036488	10.764091	3.625
Fe13	6.800461	1.036599	10.764931	3.625
Fe14	6.802207	1.036283	10.783404	3.625
Fe15	6.802314	1.036333	10.784244	3.624
Fe16	6.884249	1.036482	10.817832	3.535
Fe17	6.813367	1.034742	10.689358	3.612
Fe18	6.81285	1.034649	10.687679	3.612
Fe19	6.810994	1.033582	10.647373	3.612
Fe20	6.811353	1.033857	10.648213	3.612
Fe21	6.881466	1.036702	10.754855	3.535
Fe22	6.814378	1.03628	10.707832	3.611
Fe23	6.813352	1.036014	10.694396	3.611
Fe24	6.883623	1.037239	10.783404	3.535
S25	6.925474	1.176796	24.222774	0.074
S26	6.925512	1.176908	24.226133	0.074
S27	6.940259	1.187114	24.694685	0.083
S28	6.938726	1.186614	24.682929	0.083
S29	6.939826	1.187612	24.668654	0.083
S30	6.938934	1.18718	24.657738	0.083
S31	6.940287	1.186689	24.684608	0.083
S32	6.940358	1.18741	24.683769	0.083
S33	6.940636	1.187734	24.665295	0.083
S34	6.940487	1.187477	24.661936	0.083
S35	6.937967	1.186074	24.674532	0.083
S36	6.936827	1.185642	24.666135	0.083
S37	6.939791	1.187697	24.686288	0.083
S38	6.939486	1.186968	24.683769	0.083
S39	6.929816	1.182118	24.335294	0.063
S40	6.929809	1.182191	24.334454	0.063
S41	6.958579	1.166601	25.144763	0.095
S42	6.958503	1.166124	25.140564	0.095
S43	6.938251	1.182135	24.67957	0.085

S44	6.938034	1.181653	24.68125	0.085
S45	6.937669	1.181782	24.672013	0.085
S46	6.937257	1.181682	24.670333	0.085
S47	6.957599	1.164546	25.129648	0.095
S48	6.957593	1.164247	25.12377	0.095
S49	6.929975	1.181571	24.331095	0.064
S50	6.929978	1.181809	24.331095	0.064
S51	6.958493	1.15975	25.091862	0.097
S52	6.959046	1.158808	25.095221	0.097
S53	6.939675	1.181796	24.693005	0.085
S54	6.939904	1.182186	24.695524	0.085
S55	6.930437	1.181943	24.339492	0.064
S56	6.930567	1.181706	24.339492	0.064

Table S3. The magnetizations of atoms in $Co_{0.8}Fe_{0.2}OOH$

No.	Atom	s	p	d	tot
1	O1	0	-0.031	0	-0.031
2	O2	0.005	0.116	0	0.121
3	O3	0	-0.03	0	-0.03
4	O4	0.005	0.112	0	0.118
5	O5	0.005	0.113	0	0.118
6	O6	0	-0.032	0	-0.032
7	O7	0.006	0.122	0	0.128
8	O8	0.006	0.093	0	0.099
9	O9	0	-0.026	0	-0.026
10	O10	0.005	0.062	0	0.067
11	O11	0.001	-0.102	0	-0.101
12	O12	0	-0.011	0	-0.011
13	O13	0.007	0.062	0	0.069
14	O14	0.003	-0.068	0	-0.065
15	O15	0.001	-0.102	0	-0.101
16	O16	0.005	0.063	0	0.068
17	O17	0	-0.019	0	-0.019
18	O18	0.004	0.032	0	0.036
19	O19	0.005	0.109	0	0.114
20	O20	0	-0.019	0	-0.019
21	O21	0.001	-0.106	0	-0.105
22	O22	0.001	-0.101	0	-0.1
23	O23	0	-0.006	0	-0.006
24	O24	0.005	0.118	0	0.123
25	O25	0	-0.011	0	-0.011
26	O26	0.001	-0.002	0	-0.001
27	O27	0.009	0.033	0	0.042
28	O28	0.008	0.032	0	0.041
29	O29	0.001	-0.001	0	0
30	O30	0.008	0.03	0	0.038
31	O31	0.003	0.001	0	0.004
32	O32	0	0	0	0.001
33	O33	0.013	0.043	0	0.055
34	O34	0.004	0.002	0	0.006
35	O35	0.003	0.001	0	0.004
36	O36	0.009	0.02	0	0.028

37	O37	0.001	0	0	0
38	O38	0.008	0.028	0	0.036
39	O39	0.007	0.016	0	0.023
40	O40	0	-0.003	0	-0.002
41	O41	0.003	0.003	0	0.005
42	O42	0.003	0.004	0	0.007
43	O43	0	0	0	0
44	O44	0.008	0.029	0	0.037
45	O45	0	0.003	0	0.003
46	O46	0	-0.001	0	-0.001
47	O47	0.009	0.02	0	0.029
48	O48	0	-0.001	0	0
49	O49	0.009	0.03	0	0.039
50	O50	0.008	0.03	0	0.038
51	Co1	0.002	0.001	0.056	0.059
52	Co2	0.004	0.001	0.093	0.098
53	Co3	0.004	0.001	0.092	0.098
54	Co4	0.002	0.001	0.055	0.058
55	Co5	0.004	0.001	0.093	0.098
56	Co6	0.002	0.001	0.052	0.055
57	Co7	0.002	0.001	0.042	0.045
58	Co8	0.004	0.001	0.087	0.091
59	Co9	0	0.001	-0.03	-0.029
60	Co10	0.003	0.002	0.066	0.072
61	Co11	0.014	0.011	1.684	1.709
62	Co12	0.001	0.001	-0.036	-0.034
63	Co13	0.004	0.001	0.073	0.078
64	Co14	0.004	0.001	0.078	0.083
65	Co15	0.002	0.001	0.042	0.045
66	Co16	0.003	0.004	-0.019	-0.012
67	Co17	0	0	-0.033	-0.032
68	Co18	0	0.001	-0.037	-0.037
69	Co19	0.004	0.001	0.083	0.088
70	Co20	0.003	0.001	0.079	0.084
71	H1	0.001	0	0	0.001
72	H2	0.002	0.001	0	0.003
73	H3	0.002	0.001	0	0.003
74	H4	0.001	0	0	0.001
75	H5	0.003	0.001	0	0.003
76	H6	0.001	0	0	0.001
77	H7	0	0	0	0
78	H8	0.005	0.001	0	0.005
79	H9	0.002	0	0	0.002
80	H10	0.001	0	0	0.001
81	H11	0.004	0	0	0.004
82	H12	0	0	0	0.001
83	H13	0.003	0.001	0	0.003
84	H14	0.372	0	0	0.372
85	H15	0.001	0	0	0.001
86	H16	0	0	0	0.001
87	H17	0.001	0	0	0.001
88	H18	0	0	0	0
89	H19	0.003	0.001	0	0.003
90	H20	0	0	0	0
91	H21	0.001	0	0	0.001

92	H22	0.004	0	0	0.004
93	H23	0.001	0	0	0.001
94	H24	0.002	0.001	0	0.003
95	H25	0.003	0.001	0	0.003
96	Fe1	0.017	0.016	2.876	2.91
97	Fe2	0.02	0.063	4.077	4.16
98	Fe3	0.019	0.044	4.023	4.086
99	Fe4	0.02	0.059	4.084	4.163
100	Fe5	0.017	0.016	2.864	2.898
Accumulated Magnetizations		0.748	0.894	20.444	22.088

Table S4. The magnetizations of atoms in supported CoFeOOH by Fe_3S_4

No.	Atom	s	p	d	tot
57	Co1	0.005	0.003	0.443	0.451
58	Co2	0.004	0.003	0.238	0.245
59	Co3	0.007	0.005	0.652	0.663
60	Co4	0.013	0.023	2.609	2.645
61	Co5	0.002	0.001	0.079	0.082
62	Co6	0.012	0.014	2.659	2.685
63	Co7	0.014	0.015	2.672	2.701
64	Co8	0.004	0.003	0.146	0.153
65	Co9	0.004	0.003	0.802	0.809
66	Co10	0	0.001	0.076	0.077
67	Co11	0.003	0.001	0.215	0.219
68	Co12	0.009	0.008	0.971	0.987
69	Co13	0.013	0.015	2.622	2.65
70	Co14	0.001	0	0.09	0.092
71	Co15	0.004	0.002	0.365	0.371
72	Co16	0.002	0.001	0.097	0.101
73	Co17	0.002	0.001	0.074	0.077
74	Co18	0.006	0.004	0.78	0.79
75	Co19	0.003	0.001	0.313	0.317
76	Co20	0.011	0.015	2.63	2.656
77	H1	0.003	0.001	0	0.003
78	H2	0.005	0	0	0.005
79	H3	0.001	0	0	0.001
80	H4	0.005	0.001	0	0.006
81	H5	0.008	0.001	0	0.009
82	H6	0.003	0.002	0	0.005
83	H7	0.005	0.002	0	0.006
84	H8	0.003	0.002	0	0.005
85	H9	0.004	0.001	0	0.004
86	H10	0.004	0	0	0.004
87	H11	0	0	0	0
88	H12	0.003	0.001	0	0.003
89	H13	0.004	0.001	0	0.005
90	H14	0.007	0.002	0	0.008
91	H15	0.004	0.001	0	0.005
92	H16	0	0	0	0
93	H17	-0.002	0	0	-0.002
94	H18	0	0	0	0
95	H19	0.002	0	0	0.002

96	H20	0.004	0.002	0	0.005
97	H21	0.001	0.001	0	0.002
98	H22	-0.002	0	0	-0.002
99	H23	0.002	0.001	0	0.003
100	H24	0.005	0.001	0	0.006
101	H25	0.004	0	0	0.004
102	O1	0.008	0.035	0	0.043
103	O2	0.013	0.165	0	0.178
104	O3	0.014	0.003	0	0.017
105	O4	0.002	-0.077	0	-0.075
106	O5	0.002	-0.009	0	-0.007
107	O6	0.006	-0.059	0	-0.052
108	O7	0.016	0.054	0	0.069
109	O8	0.013	0.103	0	0.116
110	O9	0.017	0.076	0	0.093
111	O10	0.012	0.219	0	0.232
112	O11	0.014	0.065	0	0.079
113	O12	0.014	0.189	0	0.203
114	O13	0.016	0.064	0	0.08
115	O14	0.014	0.182	0	0.197
116	O15	0.016	0.069	0	0.085
117	O16	0.005	0.115	0	0.121
118	O17	0.013	0.023	0	0.036
119	O18	0.009	0.013	0	0.022
120	O19	0.01	0.011	0	0.022
121	O20	0.006	0.033	0	0.039
122	O21	-0.001	-0.008	0	-0.009
123	O22	0.006	-0.021	0	-0.015
124	O23	0.01	0.019	0	0.028
125	O24	0.011	0.047	0	0.057
126	O25	0.009	0.031	0	0.04
127	O26	0.015	0.15	0	0.165
128	O27	0.02	0.078	0	0.098
129	O28	0.012	0.172	0	0.185
130	O29	0.013	0.056	0	0.069
131	O30	0.012	0.14	0	0.152
132	O31	0.004	0.004	0	0.008
133	O32	0.015	0.167	0	0.182
134	O33	-0.007	-0.032	0	-0.039
135	O34	0	-0.175	0	-0.175
136	O35	0.001	-0.007	0	-0.005
137	O36	0.002	-0.044	0	-0.041
138	O37	0.004	-0.01	0	-0.006
139	O38	0.012	-0.015	0	-0.003
140	O39	0.015	0.073	0	0.088
141	O40	0.005	0.148	0	0.153
142	O41	0.007	0.02	0	0.027
143	O42	0.006	0.036	0	0.042
144	O43	-0.004	-0.029	0	-0.034
145	O44	0.01	-0.095	0	-0.086
146	O45	0.008	0.035	0	0.043
147	O46	-0.002	-0.165	0	-0.167
148	O47	0.016	0.052	0	0.067
149	O48	0.013	0.086	0	0.099
150	O49	0.009	0.016	0	0.025

151	O50	0.008	0.025	0	0.033
152	Fe1	0.016	0.032	4.145	4.192
153	Fe2	0.02	0.037	4.175	4.232
154	Fe3	0.02	0.035	4.168	4.223
155	Fe4	-0.016	-0.044	-4.078	-4.138
156	Fe5	0.017	0.033	4.145	4.195
		0.698	2.26	31.088	34.041

Reference

[1] F. Rong, J. Zhao, Q. Yang, C. Li, *RSC Advances* **2016**, 6, 74536.

[2] a)Y. Surendranath, M. W. Kanan, D. G. Nocera, *J. Am. Chem. Soc.* **2010**, 132, 16501; b)C. Roy, B. Sebok, S. B. Scott, E. M. Fiordaliso, J. E. Sørensen, A. Bodin, D. B. Trimarco, C. D. Damsgaard, P. C. K. Vesborg, O. Hansen, I. E. L. Stephens, J. Kibsgaard, I. Chorkendorff, *Nat. Catal.* **2018**, 1, 820.